

AN ABSTRACT OF THE THESIS OF

William Alan Eklund for the Master of Science  
(Name) (Degree)

in Oceanography presented on August 9, 1973  
(Major) (Date)

Title: A MICROPROBE STUDY OF METALLIFEROUS SEDIMENT  
COMPONENTS

Abstract approved: Redacted for privacy  
Jack Dymond

Examination of polished sections of manganese micronodules from metalliferous sediments from the Bauer Deep reveals sequences of ferromanganese deposition which are consistent for micronodules from a single sediment sample and imply a common depositional history for members of such assemblages. The relatively simple 'stratigraphy' of manganese micronodules, as compared to macronodules, makes stratigraphic correlation of depositional histories easier and more conclusive for micronodules than macronodules.

Quantitative microprobe analysis and X-ray microdiffraction patterns indicate that the major authigenic silicate component of metalliferous sediment is an iron- and magnesium-rich, low-aluminum nontronite.

Microprobe and X-ray microdiffraction analyses of manganese micronodules establish todorokite as the predominant crystalline

component. Comparison of the distributions of lanthanum, cerium, and samarium in micronodules and phosphatic fish debris indicates that bulk sediment REE distribution is determined by the relative abundances of cerium-enriched micronodules and cerium-depleted biogenic phosphate.

A Microprobe Study of  
Metalliferous Sediment Components

by

William Alan Eklund

A THESIS

submitted to

Oregon State University

in partial fulfillment of  
the requirements for the  
degree of

Master of Science

June 1974

APPROVED:

Redacted for privacy

---

Associate Professor of Oceanography  
in charge of major

Redacted for privacy

---

Dean of School of Oceanography

Redacted for privacy

---

Dean of Graduate School

Date thesis is presented August 9, 1973

Typed by Marjorie Hay for William Alan Eklund

## ACKNOWLEDGEMENTS

I am indebted to Dr. Jack Dymond, my advisor, for his patience and encouragement during the course of this work. Drs. Jack Corliss and Ross Heath also contributed valuable guidance and criticism.

Dr. Daniel Weill generously made available the microprobe facilities. Dr. Ronald Sorem kindly helped with the X-ray diffraction work. Dave Pitzl and the Center for Microscopic Studies of Washington State University, Pullman, helped obtain the SEM photos.

Discussions with John Kendrick, Dave Rea, Gordon McKay, and Dave Pitzl were valuable and are appreciated.

This work was supported by the National Science Foundation through the International Decade of Ocean Exploration, Nazca Plate Project (contract no. GX-28675).

## TABLE OF CONTENTS

	<u>Page</u>
INTRODUCTION	1
METHODS	4
Sample	4
Sample Preparation	5
Microprobe Operating Conditions	5
Quantitative Microprobe Techniques	7
MICROSCOPE OBSERVATIONS	11
Petrographic Descriptions	11
Scanning Electron Microscope Studies	16
QUALITATIVE MICROPROBE ANALYSIS	17
QUANTITATIVE MICROPROBE ANALYSIS	25
X-RAY DIFFRACTION ANALYSIS	41
DISCUSSION	44
Smectite	44
Micronodules	55
Morphology	55
Mineralogy - Todorokite	58
Mineralogy - Micro-laminated Rind	60
Chemistry	63
Rare-Earth Element Distributions	67
CONCLUSIONS	70
BIBLIOGRAPHY	74

## LIST OF FIGURES

<u>Figure</u>		<u>Page</u>
1	Photomicrographs of polished thin section of sample AII 54-14.	12
2	Scanning electron photomicrographs of a smectite aggregate and a micronodule.	18
3	Electron beam scan photographs of a micronodule.	21
4	Electron beam scan photographs of two micronodules.	23
5	X-ray diffraction patterns.	42
6	Comparison of major element concentrations.	47
7	Major element relationships.	62
8	Element distributions in todorokite and iron-rich rinds.	64
9	La and Ce concentrations.	68

## LIST OF TABLES

<u>Table</u>		<u>Page</u>
1	Microprobe Operating Conditions	7
2	Standards for Quantitative Microprobe Analysis	10
3	Micronodule Morphologies Observed in Sample AII 54-14	15
4	Elemental Concentrations, Calculated as Oxide Weight Percent	26
5	Elemental Compositions, Normalized to Constant Totals	33
6	Distribution of Cations Per Lattice Unit in Smectite	49

## A Microprobe Study of Metalliferous Sediment Components

### INTRODUCTION

Recent interest in the metalliferous sediments of the East Pacific Rise and the Bauer Deep has resulted in a profusion of chemical, isotopic, and mineralogical data on these deposits. In order to complement existing information, this study applies the techniques of reflected light microscopy, X-ray diffraction, and electron microprobe analysis to coarse fraction separates of a metalliferous sediment sample from the Bauer Deep. Previous interpretations have relied largely upon bulk chemical and mineralogical analyses despite the reported presence of coarse sediment components such as silicate aggregates, manganese micronodules, palagonite, fish debris, volcanic glass, and calcareous and siliceous biogenic remains (Dasch et al., 1971). This study concentrates on three of these components: micronodules, smectite aggregates, and phosphatic fish debris. These particular components were chosen because of the authigenic nature of the micronodules and smectite grains and the apparent concentration of rare earth elements in the fish debris suggested by bulk analyses (Dymond et al., 1973).

Despite their common occurrence in pelagic sediments, manganese micronodules have received far less attention than the more

conspicuous manganese nodules, crusts, and slabs. Micronodules are generally less than 1 mm in diameter and are disseminated sediment components whereas nodules are generally larger than 5 mm and are primarily a surface deposit (Menard, 1964). Although the external morphologies of nodules and micronodules are often similar, the bimodal size distribution of manganese concretions may reflect a genetic difference between nodules and micronodules. The distinction between micronodules and nodules or crusts is usually discounted despite their different modes of occurrence (Menard, 1964).

Concentration of micronodules by winnowing or because of slow sedimentation rates may result in crusts or agglomerates of cemented micronodules (Revelle et al., 1955). Andruschenko and Skornyakova (1969) have described concretions of cemented aggregates of small manganese globules in a matrix of iron hydroxides. The sizes of these individual globules varied from 5 to 50 microns, similar to the sizes of the disseminated micronodules observed in this study.

Chemical analyses of manganese micronodules have previously been performed either upon collections of micronodules large enough to be hand picked or have been inferred from selective leaching experiments (cf. El Wakeel and Riley, 1961; Chester and Hughes, 1967). The former technique is subject to the same criticism as the analysis of manganese nodules; that the partitioning of elements between several ferromanganese minerals within the nodule or

collection of micronodules is unknown and therefore the analysis is difficult to interpret. Inclusion of clastic debris and nuclei may also distort the bulk composition. The selective leaching technique is further limited because it fails to differentiate ferromanganese minerals comprising the micronodules and also fails to isolate micronodules from fine-grained iron oxide components or adsorbed species on insoluble minerals. These problems can be avoided by using the electron microprobe which is particularly suited to an investigation of micronodules because it is capable of analyzing individual mineral phases.

The smectite aggregates found in Bauer Deep sediments are translucent microcrystalline grains ranging in color from lemon yellow to yellow-orange. Slow-scan X-ray diffraction with digital filtering and differential peak stripping techniques identifies the mineral as a moderately well-crystallized smectite that differs from normal pelagic smectites in its unusually strong 002 and 004 reflections (Dymond *et al.*, 1973). Bulk analyses of acid leached clay mineral ( $< 2\mu$ ) residues of metalliferous sediments show high Fe/Al ratios suggestive of iron-rich smectite in the fine fraction (J. Kendrick and D. Rea, written communication, 1972). Bischoff and Sayles (1972) were unable to obtain X-ray diffraction patterns of Bauer Deep silicates with conventional methods, but tentatively identified the silicate aggregates as nontronitic montmorillonite on

the basis of refractive index measurements. Quantitative microprobe analysis of these aggregates allows the direct determination of their compositions without resort to inferences based on analyses of fine fractions of the sediment.

## METHODS

### Sample

The sediment sample chosen for study was taken from the 467-478 cm level of piston core AII 54-14, collected by R/V Atlantis II in the Bauer Deep (9°S, 102°W). This particular sample was chosen because complementary data from previous investigations are available and because the sample proved particularly amenable to preparation for microprobe work. Evidence of significant diagenesis in this sample (Dasch et al., 1971) made investigation of the authigenic components attractive. Other samples from the Bauer Deep and the East Pacific Rise were prepared for reflected light examination but proved too hydrous and friable for microprobe analysis.

The sample consists of non-calcareous, very dark brown metalliferous sediment (Bischoff and Sayles, 1972). Eh measurements indicate a mildly oxidizing environment (+200 mv) (Bischoff and Sayles, 1972). The topographic setting of the Bauer Deep between the East Pacific Rise and the fossil Galapagos Rise (Herron,

1972) effectively shields it from inputs of terrigenous debris from South America. Detailed X-ray diffraction analysis of bulk sediment by Dasch et al. (1971) reveals the presence of 'smectite,'  $\delta$ -MnO<sub>2</sub>, goethite, todorokite, and barite; as well as trace amounts of quartz, feldspar, calcite, and apatite.

### Sample Preparation

Coarse fractions were isolated by wet sieving raw sediment through a 62 micron sieve. Magnetic and heavy liquid separations were used to concentrate micronodules where necessary. Sample AII 54-14 was donated by Fred Sayles and was the only sample used for microprobe analysis. Unlike the other samples, AII 54-14 had been sieved at 20 microns. Brief ultrasonic agitation was applied when necessary to facilitate sieving.

Polished thin sections were prepared from epoxy grain mounts of each sample. Polished thin sections can be used for both transmitted and reflected light microscopy and microprobe analysis. Final polishing was with  $\frac{1}{4}$  micron diamond grit. For microprobe analysis sections were carbon coated.

### Microprobe Operating Conditions

All microprobe work was performed on an Applied Research Laboratories microprobe with a takeoff angle of 52.5°. The electron

beam diameter was fixed at 20 microns for all quantitative work. A 20 micron beam minimizes specimen deterioration caused by overheating and also allows return to a known location for multiple analyses. The presence of minute fractures and pits in the surfaces of many of the mineral phases examined required that a large beam, which effectively excites an integrated X-ray emission from the entire area of the beam, be used if more than three elements were to be quantitatively determined. Since the three detectors of the ARL system can only monitor three elements at once, the beam must be returned to a precise location on the specimen after each cycle if more than three elements are to be analyzed. Hence, a sample inhomogeneous on a 1 micron scale is very difficult to analyze with a 1 micron diameter beam, but can be satisfactorily analyzed with a 20 micron beam.

Integration times varied from 30 seconds to 120 seconds, depending on the concentration of the element being analyzed. For each element, the integration times were identical for standard and unknown.

Electron beam operating conditions for each of the 19 elements analyzed are listed in Table 1.

Table 1. Microprobe Operating Conditions.

Element	Accelerating Voltage (Kv)	Sample Current (Nanoamps)	Integration Time (sec)
Na	15	50	30
K	15	50	30
Ca	15	50	30
Fe	15	50	30
Si	15	50	30
Mg	15	50	30
Ti	15	50	60
S	15	50	60
Al	15	50	60
Ni	15	50	90
P	15	50	90
Zn	15	50	90
Co	15	50	90
Cu	15	50	90
Mn	15	50	90
Ba	30	100	120
La	20	100	120
Ce	20	100	120
Sm	30	100	120

### Quantitative Microprobe Analysis

Quantitative microprobe determination of elemental concentrations are based on comparison of characteristic X-ray intensities measured on standards and unknowns. Raw intensity data is corrected for background, beam current drift, detector deadtime error, and matrix effects. Matrix effects include X-ray generation and absorption of both characteristic and continuous fluorescence. The individual and combined correction factors necessary for

quantitative analysis are described by Sweatman and Long (1969) and are calculated with a program (EMPADR VII) written by Rucklidge and Gasparrini (1968). After background removal and correction of raw intensity data for beam current drift and deadtime error, the complete correction formula, as given by Sweatman and Long (1969) becomes:

$$C_{\text{unknown}} = C_{\text{std}} \times \frac{I_u}{I_s} \times \left[ \begin{array}{cc} \text{generation or} & \text{absorption} \\ \text{atomic number} & \text{factor} \\ \text{factor} & \end{array} \right]$$

$$\left[ \begin{array}{cc} \frac{R_s}{R_u} \cdot \frac{S_u}{S_s} & \times \frac{f(\chi)_s}{f(\chi)_u} \\ \frac{(1 + \nu_s)}{(1 + \nu_u)} & \times \frac{(1 + \psi_s)}{(1 + \psi_u)} \end{array} \right]$$

$$\left[ \begin{array}{cc} \text{characteristic} & \text{continuous} \\ \text{fluorescence} & \text{fluorescence} \\ \text{factor} & \text{factor} \end{array} \right]$$

Since the four matrix correction factors are each a function of the compositions of the standard and unknown, the calculation of the correction factors is an iterative process which initially uses the apparent, uncorrected composition and terminates when successive calculations give a nearly constant composition.

Characteristic X-ray intensities measured were  $L_{\alpha}$  emissions of Ba, La, Ce, and Sm, and  $K_{\alpha}$  emissions of all other elements.

Backgrounds were measured on both sides of the characteristic peaks of both standards and unknowns. Standards were measured at the beginning and end of each run, thereby enabling a drift correction to be made for variation in beam current during a run.

Standards for quantitative microprobe work must be homogenous, well-polished, and of a precisely known composition. Ideally, standards should conform as closely as possible to the composition of the unknown specimens. However, since microprobe standards for ferromanganese oxides and smectites are not available, a set of standards was chosen from a collection generously made available by Daniel F. Weill. Fortunately, the quality of these standards and the matrix corrections applied to the data minimize errors due to differences between standard and specimen compositions. Pure metallic standards were chosen for the minor transition metals because it is difficult to prepare a microprobe standard of an element with a low ( $< 1\%$ ) concentration which is both homogenous and of a precisely known composition. The precisely known composition and matrix effects favor a pure metal standard.

Standards for the other elements were minerals or synthetic glasses. Standards chosen for each element are listed in Table 2.

Table 2. Standards for Quantitative Microprobe Analysis.

---

Na	Na-feldspar
K	K-feldspar
Ca	Synthetic silicate glass
Fe	Hematite
Si	Olivine
Mg	Olivine
Ti	Synthetic Ti-Ca silicate glass
S	Barite
Al	Synthetic silicate glass
Ni	Pure Ni
P	Apatite
Zn	Pure Zn
Co	Pure Co
Cu	Pure Cu
Mn	Rhodonite
Ba	Barite
La	Synthetic glass (Drake and Weill, 1972)
Ce	Synthetic glass (Drake and Weill, 1972)
Sm	Synthetic glass (Drake and Weill, 1972)

---

## MICROSCOPE OBSERVATIONS

Petrographic Descriptions

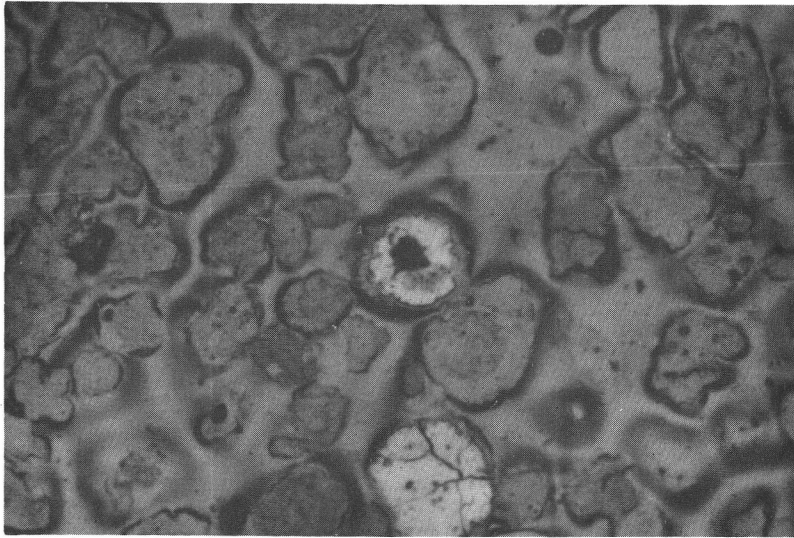
Examination of polished sections of micronodules under reflected light reveals two opaque ferromanganese phases. On the basis of X-ray diffraction and microprobe analyses, these are referred to as todorokite and an iron-rich phase. Foreign nuclei are absent from virtually all micronodules. Figure 1 shows photomicrographs of a polished grain mount containing both manganese micronodules and smectite aggregates from sample AII 54-14. The three photos were taken in reflected, reflected polarized, and transmitted light, respectively.

The todorokite typically occurs as globular spherules 5 to 100 microns in diameter (two are visible in photos in Figure 1). They are characterized by high reflectivity and well-defined radial anisotropy. Microhardness tests indicate a hardness greater than that of steel. High power (1300X) oil immersion examination of polished sections reveals a homogeneous, radially striated phase with micro-inclusions of unidentifiable impurities. Fractures, both radial and concentric, are common and may be caused by either sample preparation and dessication or natural autoclastic processes.

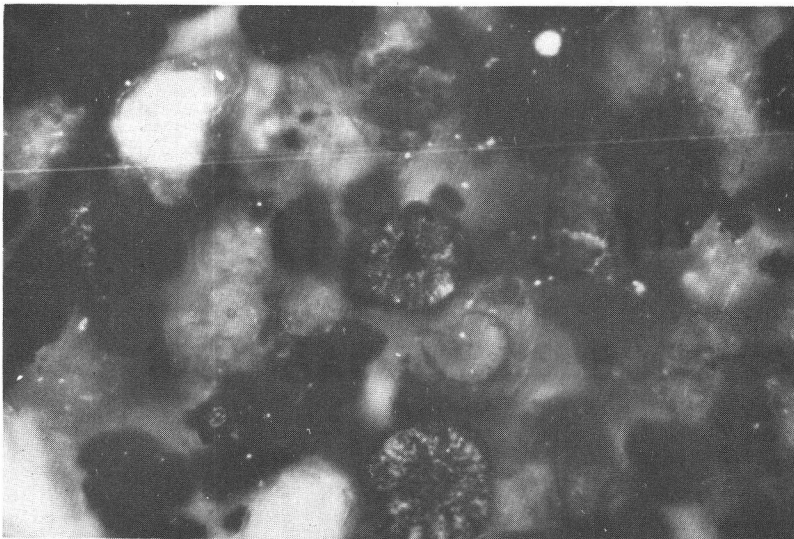
The iron-rich phase is poorly reflective, soft, and apparently isotropic. Rounded grains are most common, but no particular

Figure 1. Photomicrographs of a polished thin section of coarse grains from 467 to 478 cm in core AII 54-14. (a) Reflected light. (b) Reflected polarized light. (c) Transmitted light.

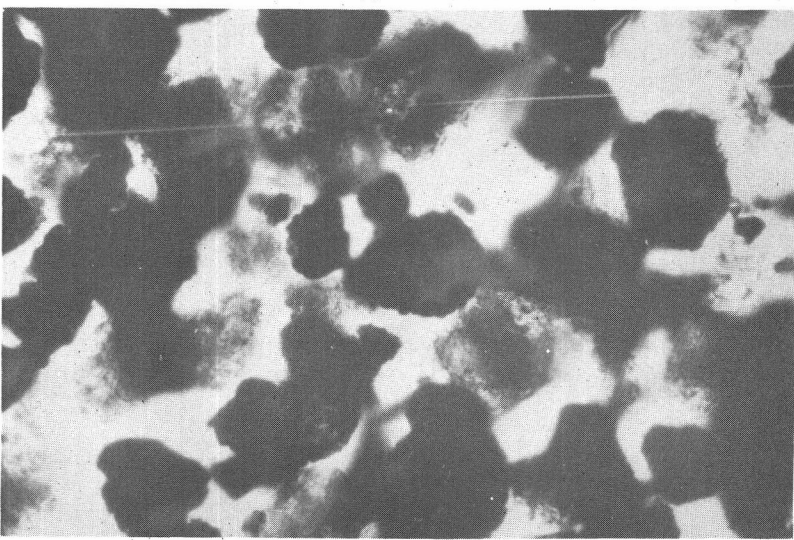
A



B



C



100  $\mu$ m

morphology is evident, possible because of damage during collection and preparation. Although apparently homogeneous under lower magnifications, high power (1300X) oil immersion examination of polished sections reveals concentric and cusped micro-laminations of unidentifiable components which exhibit colors ranging from varying shades of gray to light brown. The width of the micro-laminations is typically less than 1 micron, precluding the identification of component phases by optical means. Occasional highly reflective lamellae point to the presence of a mineral with similar optical reflectivity to todorokite, but the scale of the lamellae prevents positive identification.

Although the iron-rich phase is most abundant, micronodules comprised solely of todorokite, as well as micronodules with several morphological combinations of the two types of depositional phases are common. Tabulation of the types of morphology observable in the polished sections suggests that the ferromanganese precipitates formed in a sequence that was common to most of the micronodules from in a particular sediment sample. The genetic sequence is todorokite deposition followed by deposition of the iron-rich phase. A compilation of morphologies in 412 micronodules from sample AII 54-14 is given in Table 3. As indicated, 90 percent of the micronodules examined are either homogeneous iron-rich grains or todorokite cores rimmed with the iron-rich phase. The presence of

a small number of micronodules composed of multiple laminations of massive todorokite and micro-laminated iron-rich phase indicates that both deposits are authigenic, and resemble phases found in typical oceanic macronodules. Other morphological types are rare in the AII 54-14 sample. They include grains consisting of crenulated intergrowths of massive todorokite and the iron-rich phase, and grains of smectite aggregate with a rind of todorokite or iron-rich phase.

Table 3. Micronodule Morphologies Observed in Sample AII 54-14.

	Number	Percent
Micro-laminated iron-rich micronodules	280	68%
Todorokite core with iron-rich rind	87	22
Irregularly crenulated intergrowth	17	4
Multiply laminated	13	3
Todorokite with smectite rind	5	1
Iron-rich core with todorokite rind	<u>3</u>	<u>1</u>
Total	412	99%

Micronodules from other core samples from the Bauer Deep and the East Pacific Rise do not generally have the same morphology or sequence of deposition of todorokite and the iron-rich phase as those in sample AII 54-14, but tend to be uniform within a sample. In some samples, only homogeneous micronodules are present; in

others most micronodules contain nuclei of translucent yellow smectite; and in others, micronodules with multiple large laminations predominate. The micro-laminated, iron-rich material is present in all micronodule samples, but the massive, homogeneous todorokite phase is not always present. Further work is needed to define the regional and temporal distributions of the various micronodules morphologies.

The smectite aggregates appear as lemon-yellow to yellow-orange microcrystalline grains in transmitted light. A few pseudomorph foraminifera tests or encrust radiolarian tests. Examination of polished grain mounts under high power reveals only yellow microcrystals without visible internal structure.

#### Scanning Electron Microscope Studies

Surface textures of manganese micronodules and smectite grain aggregates were examined with a scanning electron microscope (SEM). Figure 2 shows SEM photographs of a single smectite grain, possibly a pseudomorph after a foraminifera, and a single micronodule. In both cases, the surface textures are characteristically delicate and porous. The delicately bladed, ribbon-like habit of the crystals on the surface of the smectite grain is similar to the habit of nontronite and montmorillonite (Dave Pitzl, oral communication, 1973). Because of the similarities in crystal habit of these two

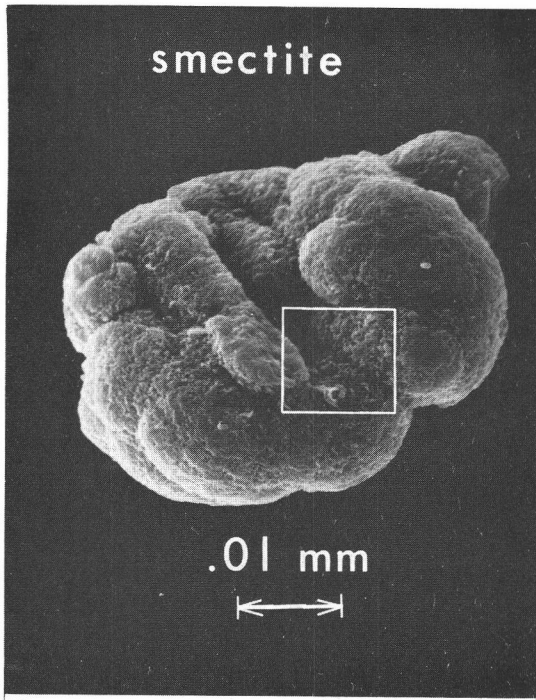
smectite species, absolute identification on the basis of the SEM photos is not possible.

The manganese micronodule is abraded on its exposed surfaces (Figure 2), but a characteristically porous texture is apparent on the more protected surfaces. The closed-cell, porous network is characteristic of an oxide structure, but further identification is not feasible (Dave Pitzl, oral communication, 1973).

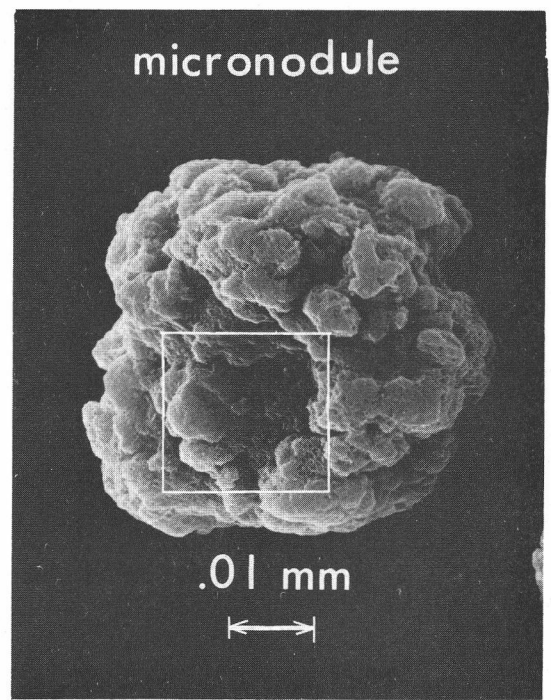
#### QUALITATIVE MICROPROBE ANALYSIS

Electron beam scans were used to qualitatively determine the distribution of iron and manganese in polished micronodules. In these scans the electron beam, focused to a diameter of less than 1 micrometer, was swept systematically across the sample while a synchronous oscilloscope monitored the intensity of either backscattered electrons or characteristic Fe or Mn radiation. In the area scan mode the beam was swept in a raster pattern over a square area and the areal distribution of X-ray intensity or backscattered electrons displayed on the oscilloscope. In the line scan mode, the beam was swept in a line across the specimen and the monitored X-ray intensity was displayed on the Y-axis of the oscilloscope as the position of the beam on the specimen was displayed on the X-axis. The result is a profile which approximates the concentration of Mn or Fe as a function of position.

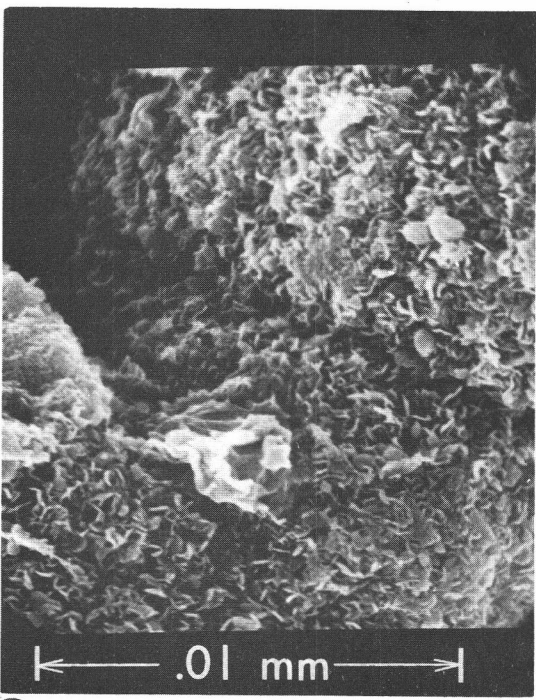
Figure 2. Scanning electron photomicrographs. (a) and (c): Smectite aggregate, possibly a pseudomorph after a foraminifera test. (b) and (d): Manganese micronodule. Accelerating potential 20 Kv.



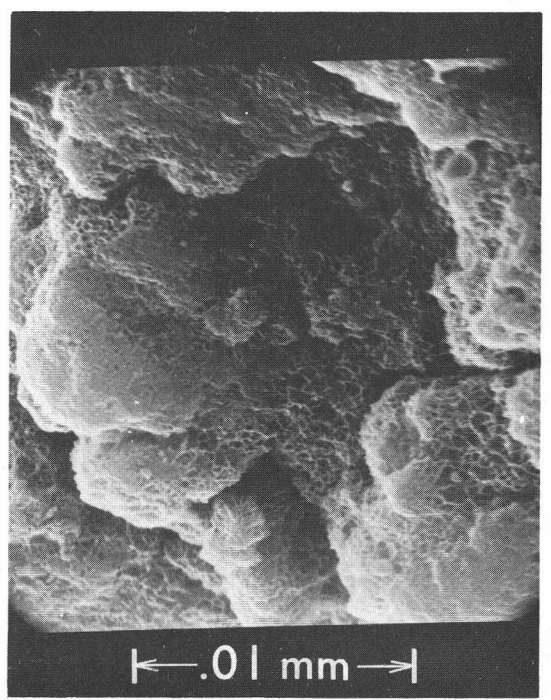
A



B



C



D

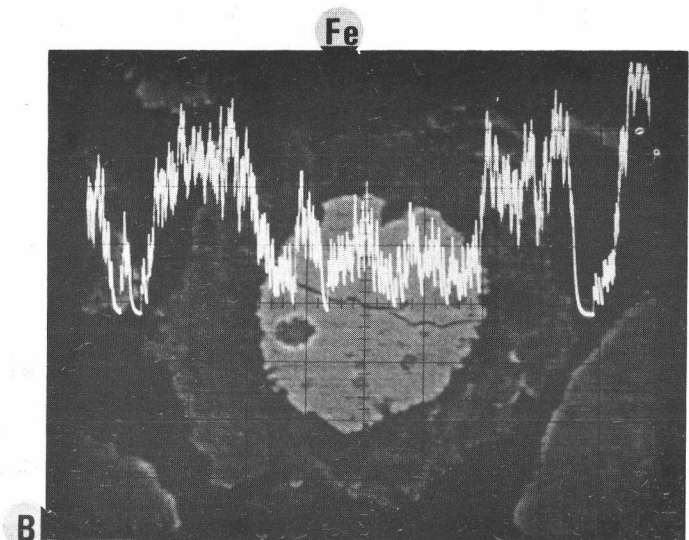
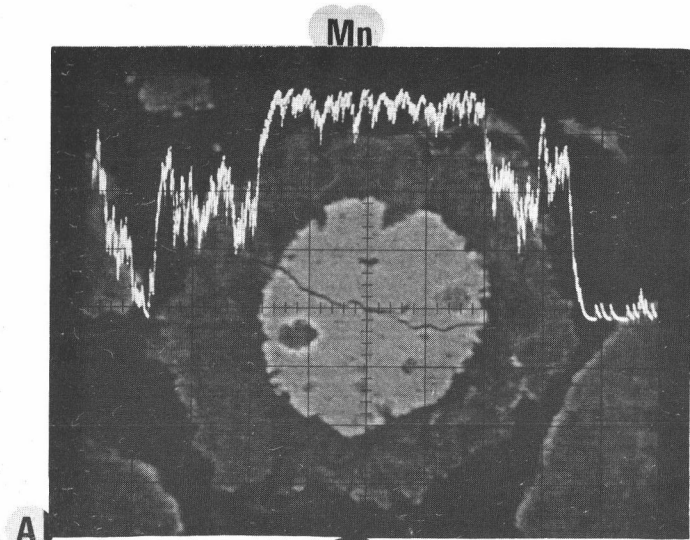
Backscattered electron intensity is approximately proportionate to the average atomic number distribution in the specimen. It is similar to the optical appearance of the specimen.

Figures 3 and 4 are beam scan photos of three micronodules. Line scan profiles of manganese (3a) and iron (3b) concentrations are superimposed on backscattered electron photos of the specimen traversed. In each photo, the base of the profile lies over the traverse line of the specimen. Figures 3(c) and (d) show area scan photos of the same specimen. In each photo the field of view is 85 x 68 micrometers.

Each of the micronodules in Figures 3 and 4 contain manganese-rich todorokite cores with iron-rich, micro-laminated rinds. The micro-laminations in the rind are not resolvable in these photos. The contrast in backscattered electron intensity between the todorokite and the iron-rich rinds primarily reflects differences in porosity between the two materials.

In the lower right corner of the photos in Figure 3 is a nontronite grain. Although it displays a backscattered electron intensity similar to that of the iron-rich rind, the line scan profiles and the area scan photos clearly show the different manganese concentrations in these phases.

Figure 3. Electron beam scan photographs. Photo areas are 85 x 68 microns. (a) and (b): Line scan profiles of Mn (a) and Fe (b) superimposed on backscattered electron distribution. (c) and (d): Area scans of Mn (c) and Fe (d) distributions.



50  $\mu$ m

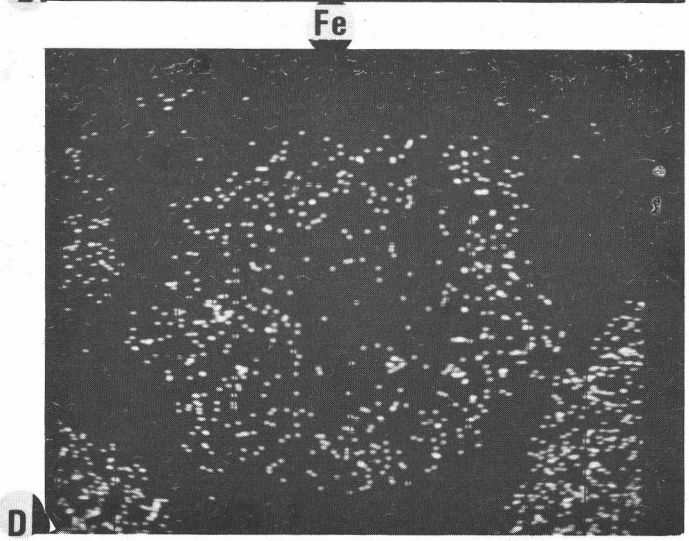
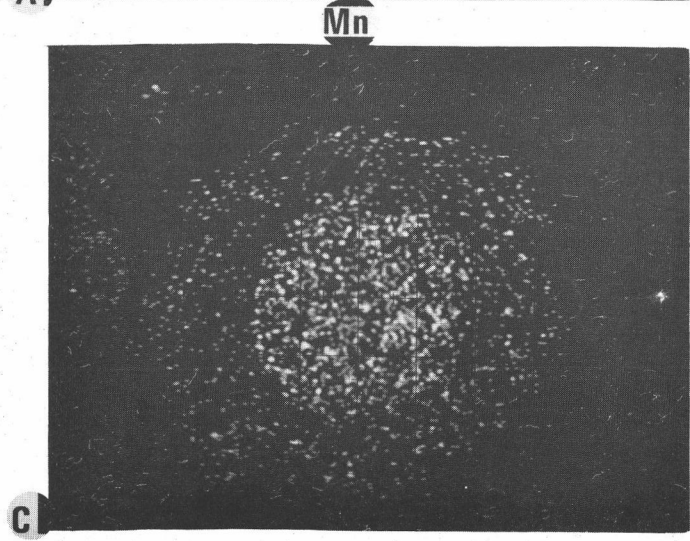
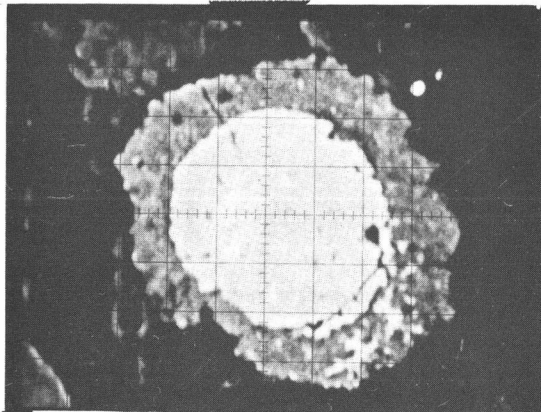


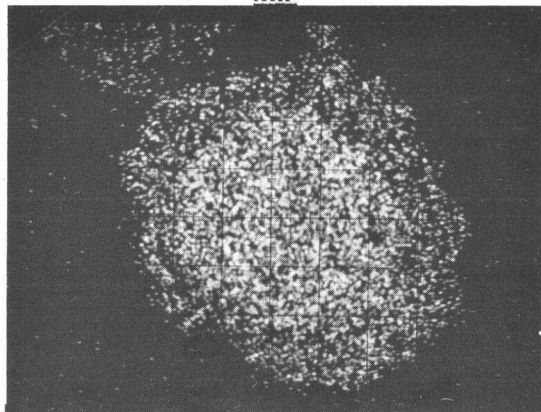
Figure 4. Electron beam area scan photos of two micro-nodules. (a) and (b): Backscattered electrons. (c) and (d): Mn distribution. (e) and (f): Fe distribution. Photo areas are 85 x 68 microns.

B.S.E.



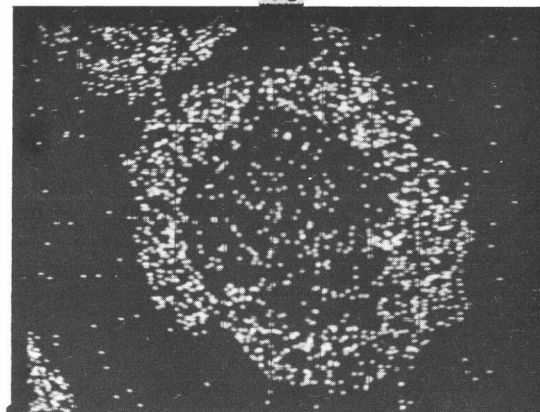
A

Mn



C

Fe

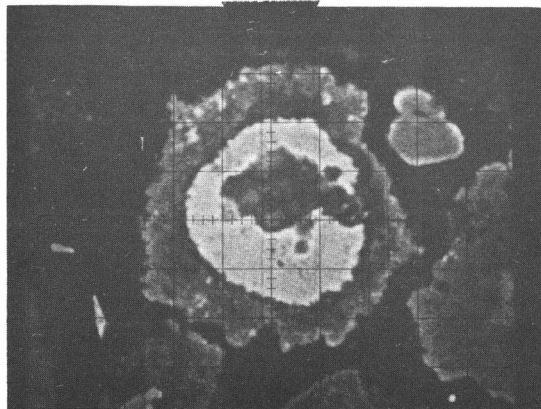


E

50  $\mu$ m

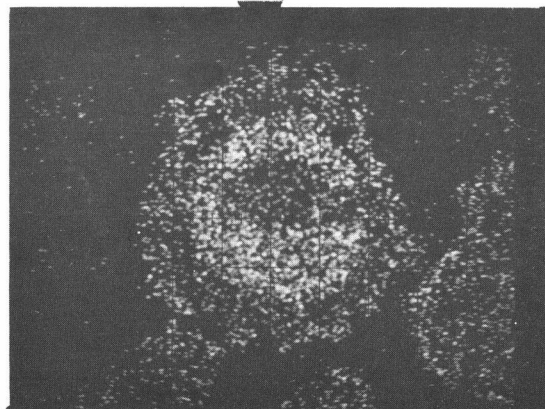
Mn

B.S.E.



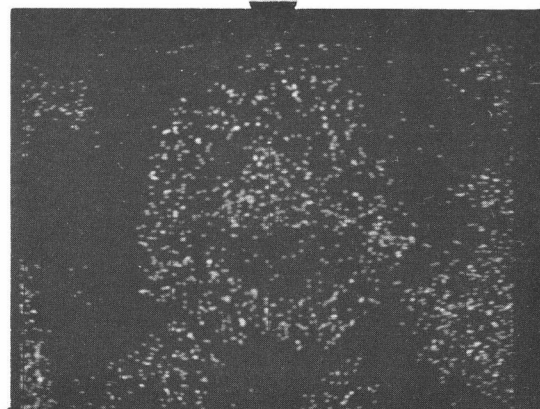
B

Mn



D

Fe



F

## QUANTITATIVE MICROPROBE ANALYSIS

Twenty-eight mineral grains were quantitatively analyzed for each of the 19 elements listed in Table 1. The grains analyzed included eleven smectite grains, five grains of phosphatic fish debris, and six each of the two types of ferromanganese deposits. Grains were chosen for analysis on the basis of surface polish and homogeneity, thereby minimizing the effects of microscopic pits, fractures, and mineral inclusions.

Results are calculated as oxide weight percents and are presented in Table 4. Precision, as determined from counting statistics, is presented for one sample of each of the four phases analyzed. Partial duplicate analyses for one smectite grain and one micronodule are also presented.

Since the X-ray data can only be used to determine elemental concentrations, the oxide species assigned to each element must be assumed. Calculation of the weight percentage of each oxide is therefore dependent on the assigned oxide species and may differ from the actual oxide weight. Thus, the oxide weight percent of iron calculated as goethite,  $\text{FeO(OH)}$ , is higher than that calculated as hematite,  $\text{Fe}_2\text{O}_3$ .

Table 4 shows that the sum of the oxide weight percents does not approach 100 in most cases. Assignment of heavier oxide species

Table 4. Elemental Concentrations, Calculated as Oxide Weight Percents.

(a) Smectite grains

	#1 $\pm 1\sigma$	#1 <sup>(2)</sup>	#2	#3	#4	#5
CaO	.40 $\pm$ .01 <sup>(1)</sup>	.43	.35	.49	.25	.44
K <sub>2</sub> O	1.97 $\pm$ .03	2.11	1.91	1.39	2.01	1.48
Na <sub>2</sub> O	.70 $\pm$ .02	.51	.41	.34	.40	.37
Fe <sub>2</sub> O <sub>3</sub>	30.45 $\pm$ .12	30.72	27.71	20.73	24.49	23.12
SiO <sub>2</sub>	52.00 $\pm$ .23	51.80	46.95	33.68	49.77	35.97
MgO	5.73 $\pm$ .04	5.62	4.80	4.20	5.85	4.28
TiO <sub>2</sub>	.03 $\pm$ .01		.04	.04	.02	.03
SO <sub>3</sub>	.05 $\pm$ .02		.05	.04	.07	.02
Al <sub>2</sub> O <sub>3</sub>	2.73 $\pm$ .03	2.49	2.58	1.64	2.55	1.94
NiO	.06 $\pm$ .01		.06	.00	.15	.09
ZnO	.10 $\pm$ .03		.04	.00	.02	.00
CoO	.06 $\pm$ .01		.04	.00	.03	.00
CuO	.14 $\pm$ .02		.08	.04	.09	.00
MnO <sub>2</sub>	.38 $\pm$ .10	.30	.62	.81	.49	.74
BaO	.02 $\pm$ .01		.02	.00	.05	.00
La <sub>2</sub> O <sub>3</sub>	.00		.00	.00	.00	.00
Ce <sub>2</sub> O <sub>3</sub>	.00		.00	.00	.00	.00
Sm <sub>2</sub> O <sub>3</sub>	.00		.00	.00	.00	.00
P <sub>2</sub> O <sub>5</sub>	.08 $\pm$ .01		.12	.17	.12	.16
Total	94.90		85.78	63.57	86.36	68.64

(1) Precision based on counting statistics.

(2) Partial duplicate analysis.

Table 4. Continued.

(a) Continued.

	#6	#7	#8	#9	#10	#11
CaO	.34	.31	.40	.37	.67	.35
K <sub>2</sub> O	1.49	1.79	1.62	1.69	1.09	1.20
Na <sub>2</sub> O	.54	.63	.63	.47	.73	.39
Fe <sub>2</sub> O <sub>3</sub>	19.96	23.39	25.75	21.43	28.97	22.00
SiO <sub>2</sub>	38.43	45.75	47.26	44.23	30.39	30.15
MgO	4.78	4.89	5.37	5.39	3.24	3.90
TiO <sub>2</sub>	.00	.02	.03	.00	.09	.03
SO <sub>3</sub>	.03	.07	.08	.08	.06	.02
Al <sub>2</sub> O <sub>3</sub>	1.38	2.24	1.82	1.70	1.45	1.34
NiO	.09	.13	.15	.09	.13	.06
ZnO	.00	.00	.02	.00	.00	.00
CoO	.00	.02	.04	.00	.02	.00
CuO	.00	.03	.08	.02	.04	.00
MnO <sub>2</sub>	.76	.62	.52	.51	1.50	.62
BaO	.00	.05	.05	.09	.01	.00
La <sub>2</sub> O <sub>3</sub>	.00	.00	.00	.00	.00	.00
Ce <sub>2</sub> O <sub>3</sub>	.00	.00	.00	.00	.00	.00
Sm <sub>2</sub> O <sub>3</sub>	.00	.00	.00	.00	.00	.00
P <sub>2</sub> O <sub>5</sub>	<u>.08</u>	<u>.18</u>	<u>.13</u>	<u>.21</u>	<u>.38</u>	<u>.13</u>
Total	67.88	80.12	83.95	76.28	68.77	60.20

Table 4. Continued.

(b) Todorokite

	#1	#1 <sup>(2)</sup>	#2	#3
CaO	1.10 ± .02 <sup>(1)</sup>	1.07	1.19	1.36
K <sub>2</sub> O	1.58 ± .03	1.48	1.72	1.62
Na <sub>2</sub> O	1.07 ± .02	1.18	1.12	1.23
Fe <sub>2</sub> O <sub>3</sub>	1.22 ± .03	1.22	1.37	.80
SiO <sub>2</sub>	.62 ± .03	.43	1.31	.37
MgO	2.98 ± .03	2.94	3.13	3.03
TiO <sub>2</sub>	.02 ± .01		.03	.02
SO <sub>3</sub>	.03 ± .02		.10	.09
Al <sub>2</sub> O <sub>3</sub>	.41 ± .01	.44	.32	.20
NiO	.27 ± .02		.32	.24
ZnO	.04 ± .03		.09	.06
CoO	.00		.02	.00
CuO	.48 ± .02		.54	.55
MnO <sub>2</sub>	74.01 ± .22	69.50	73.65	74.07
BaO	1.35 ± .01		1.53	1.54
La <sub>2</sub> O <sub>3</sub>	.00		.00	.00
Ce <sub>2</sub> O <sub>3</sub>	.05 ± .01		.06	.06
Sm <sub>2</sub> O <sub>3</sub>	.02 ± .01		.02	.02
P <sub>2</sub> O <sub>5</sub>	<u>.09 ± .01</u>		<u>.09</u>	<u>.36</u>
Total	85.34		86.61	85.62

(1) Precision based on counting statistics.

(2) Partial duplicate analysis.

Table 4. Continued.

(b) Continued.

	#4	#5	#6
CaO	1.24	1.21	1.06
K <sub>2</sub> O	1.42	1.37	1.49
Na <sub>2</sub> O	1.04	.98	1.05
Fe <sub>2</sub> O <sub>3</sub>	3.02	2.03	1.26
SiO <sub>2</sub>	1.87	.88	.63
MgO	3.23	3.11	3.01
TiO <sub>2</sub>	.02	.01	.03
SO <sub>3</sub>	.03	.10	.05
Al <sub>2</sub> O <sub>3</sub>	.46	.43	.27
NiO	.40	.38	.31
ZnO	.09	.09	.07
CoO	.01	.02	.01
CuO	.60	.57	.55
MnO <sub>2</sub>	72.08	73.73	75.85
BaO	1.15	1.55	1.82
La <sub>2</sub> O <sub>3</sub>	.00	.00	.00
Ce <sub>2</sub> O <sub>3</sub>	.04	.08	.07
Sm <sub>2</sub> O <sub>3</sub>	.03	.03	.03
P <sub>2</sub> O <sub>5</sub>	<u>.10</u>	<u>.13</u>	<u>.08</u>
Total	86.83	86.70	87.64

Table 4. Continued.

## (c) Micro-laminated iron-rich grains

	#1	#2	#3	#4	#5	#6
CaO	.98 $\pm$ .02	1.22	.84	.80	1.14	1.21
K <sub>2</sub> O	.11 $\pm$ .02	.47	.15	.11	.12	.21
Na <sub>2</sub> O	.10 $\pm$ .01	.34	.14	.16	.15	.16
Fe <sub>2</sub> O <sub>3</sub>	11.61 $\pm$ .08	10.78	14.38	11.21	11.68	12.88
SiO <sub>2</sub>	6.50 $\pm$ .08	5.46	9.00	6.80	7.11	7.40
MgO	1.33 $\pm$ .02	2.93	1.59	1.20	1.50	2.53
TiO <sub>2</sub>	.06 $\pm$ .01	.15	.13	.05	.06	.12
SO <sub>3</sub>	.06 $\pm$ .01	.07	.03	.08	.19	.07
Al <sub>2</sub> O <sub>3</sub>	.65 $\pm$ .02	.95	.99	.58	.74	1.32
NiO	.20 $\pm$ .01	.57	.13	.20	.35	.61
ZnO	.05 $\pm$ .02	.26	.12	.04	.10	.21
CoO	.06 $\pm$ .01	.12	.06	.02	.06	.12
CuO	.07 $\pm$ .01	.48	.18	.07	.15	.05
MnO <sub>2</sub>	16.84 $\pm$ .06	40.32	19.15	16.50	19.59	15.78
BaO	.31 $\pm$ .01	.64	.50	.61	.63	.39
La <sub>2</sub> O <sub>3</sub>	.00	.04	.02	.00	.00	.02
Ce <sub>2</sub> O <sub>3</sub>	.01 $\pm$ .01	.06	.02	.02	.04	.04
Sm <sub>2</sub> O <sub>3</sub>	.02 $\pm$ .01	.09	.04	.03	.03	.06
P <sub>2</sub> O <sub>5</sub>	<u>.20 <math>\pm</math> .01</u>	<u>.28</u>	<u>.20</u>	<u>.28</u>	<u>.32</u>	<u>.22</u>
Total	39.16	65.23	47.67	38.76	43.96	43.40

Table 4. Continued.

(d) Phosphatic fish debris

	#1	#2	#3	#4	#5
CaO	44.98 ± .11	42.86	43.60	38.09	39.98
K <sub>2</sub> O	.08 ± .01	.06	.05	.04	.04
Na <sub>2</sub> O	.72 ± .02	.65	.73	.59	.66
Fe <sub>2</sub> O <sub>3</sub>	.36 ± .02	.30	.31	.28	.24
SiO <sub>2</sub>	.05 ± .01	.09	.07	.08	.03
MgO	.60 ± .01	.60	.62	.73	.60
TiO <sub>2</sub>	.01 ± .01	.01	.02	.00	.00
SO <sub>3</sub>	.75 ± .03	.62	.63	.68	.57
Al <sub>2</sub> O <sub>3</sub>	.07 ± .01	.05	.07	.09	.69
NiO	.00	.00	.00	.00	.00
ZnO	.01 ± .03	.00	.00	.00	.00
CoO	.00	.00	.00	.00	.00
CuO	.04 ± .02	.01	.03	.02	.06
MnO <sub>2</sub>	.35 ± .02	.24	.30	.32	.30
BaO	.00	.00	.00	.00	.00
La <sub>2</sub> O <sub>3</sub>	.24 ± .01	.22	.27	.30	.23
Ce <sub>2</sub> O <sub>3</sub>	.00	.00	.00	.00	.00
Sm <sub>2</sub> O <sub>3</sub>	.06 ± .01	.07	.07	.06	.06
P <sub>2</sub> O <sub>5</sub>	<u>34.71 ± .14</u>	<u>31.89</u>	<u>33.44</u>	<u>29.41</u>	<u>30.00</u>
Total	83.03	77.67	80.21	70.69	73.46

to some of the elements, e. g. substituting  $\text{FeO(OH)}$  for  $\text{Fe}_2\text{O}_3$ , is not sufficient to correct the low totals. This problem may result from the presence of other elements not determined, from poorly polished or scratched specimen surfaces, from high concentrations of structural water, or from the presence of voids or pores. In the grains studied, the only phase for which low totals could conceivably be due to undetermined elements is the phosphatic fish debris, in which carbonate may be a major constituent.

To permit comparison within each grain type, the compositions of the four phases have each been normalized (Table 5). The compositions of the smectite, phosphatic fish debris, and todorokite phases have each been normalized to give totals equal to that of the highest total initially obtained within each group. The compositions of the iron-rich phases are normalized to the value used for the todorokite grains to allow these two phases to be compared. This procedure is justified because the effect of surface imperfections, structural water, or porosity in a sample is to lower the apparent relative concentration of each element by the same amount. An additional justification is that the highest totals obtained for the smectite, phosphate, and todorokite phases are in accord with the values typically reported for these phases on a water-free basis.

Average normalized compositions of the four phases are also given in Table 5.



Table 5. Continued

(a) Continued

	#7	#8	#9	#10	#11
CaO	.37	.45	.46	.92	.55
K <sub>2</sub> O	2.12	1.83	2.11	1.50	1.89
Na <sub>2</sub> O	.75	.71	.58	1.01	.61
Fe <sub>2</sub> O <sub>3</sub>	27.70	29.11	26.66	39.98	34.68
SiO <sub>2</sub>	54.19	53.42	55.03	41.94	47.53
MgO	5.79	6.07	6.71	4.47	6.15
TiO <sub>2</sub>	.02	.03	.00	.12	.05
SO <sub>3</sub>	.08	.09	.10	.08	.03
Al <sub>2</sub> O <sub>3</sub>	2.65	2.06	2.11	2.00	2.11
NiO	.15	.17	.11	.18	.09
ZnO	.00	.02	.00	.00	.00
CoO	.02	.04	.00	.03	.00
CuO	.03	.09	.02	.06	.00
MnO <sub>2</sub>	.73	.59	.63	2.07	.98
BaO	.06	.06	.11	.01	.00
La <sub>2</sub> O <sub>3</sub>	.00	.00	.00	.00	.00
Ce <sub>2</sub> O <sub>3</sub>	.00	.00	.00	.00	.00
Sm <sub>2</sub> O <sub>3</sub>	.00	.00	.00	.00	.00
P <sub>2</sub> O <sub>5</sub>	<u>.21</u>	<u>.15</u>	<u>.26</u>	<u>.52</u>	<u>.20</u>
Total	94.90	94.90	94.90	94.90	94.90

Table 5. Continued.

(a) Continued

	Mean $\pm$ 1 $\sigma$	Mean $\pm$ 1 $\sigma$ (excluding #10)
CaO	.51 $\pm$ .18	.47 $\pm$ .13
K <sub>2</sub> O	1.99 $\pm$ .19	2.04 $\pm$ .11
Na <sub>2</sub> O	.64 $\pm$ .17	.60 $\pm$ .12
Fe <sub>2</sub> O <sub>3</sub>	30.63 $\pm$ 3.92	29.70 $\pm$ 2.53
SiO <sub>2</sub>	51.32 $\pm$ 3.88	52.25 $\pm$ 2.44
MgO	5.95 $\pm$ .64	6.10 $\pm$ .44
TiO <sub>2</sub>	.04 $\pm$ .03	.03 $\pm$ .02
SO <sub>3</sub>	.06 $\pm$ .02	.06 $\pm$ .02
Al <sub>2</sub> O <sub>3</sub>	2.40 $\pm$ .35	2.44 $\pm$ .34
NiO	.11 $\pm$ .05	.11 $\pm$ .05
ZnO	.02 $\pm$ .03	.02 $\pm$ .03
CoO	.02 $\pm$ .02	.02 $\pm$ .02
CuO	.05 $\pm$ .05	.05 $\pm$ .05
MnO <sub>2</sub>	.90 $\pm$ .46	.78 $\pm$ .27
BaO	.03 $\pm$ .04	.03 $\pm$ .04
La <sub>2</sub> O <sub>3</sub>	.00 $\pm$ .00	.00 $\pm$ .00
Ce <sub>2</sub> O <sub>3</sub>	.00 $\pm$ .00	.00 $\pm$ .00
Sm <sub>2</sub> O <sub>3</sub>	.00 $\pm$ .00	.00 $\pm$ .00
P <sub>2</sub> O <sub>5</sub>	.20 $\pm$ .12	.17 $\pm$ .06

Table 5. Continued.

(b) Todorokite, normalized to 87.64%

	#1	#2	#3	#4
CaO	1.12	1.20	1.39	1.25
K <sub>2</sub> O	1.62	1.74	1.66	1.43
Na <sub>2</sub> O	1.10	1.13	1.26	1.05
Fe <sub>2</sub> O <sub>3</sub>	1.26	1.39	.82	3.05
SiO <sub>2</sub>	.64	1.33	.38	1.89
MgO	3.06	3.17	3.10	3.26
TiO <sub>2</sub>	.02	.03	.02	.02
SO <sub>3</sub>	.03	.10	.09	.03
Al <sub>2</sub> O <sub>3</sub>	.42	.33	.20	.46
NiO	.28	.33	.25	.40
ZnO	.04	.09	.06	.09
CoO	.00	.02	.00	.01
CuO	.49	.55	.56	.61
MnO <sub>2</sub>	76.00	74.52	75.81	72.75
BaO	1.38	1.55	1.58	1.16
La <sub>2</sub> O <sub>3</sub>	.00	.00	.00	.00
Ce <sub>2</sub> O <sub>3</sub>	.05	.06	.06	.04
Sm <sub>2</sub> O <sub>3</sub>	.02	.02	.02	.03
P <sub>2</sub> O <sub>5</sub>	<u>.09</u>	<u>.09</u>	<u>.37</u>	<u>.10</u>
Total	87.64	87.64	87.64	87.64

Table 5. Continued.

(b) Continued

	#5	#6	Mean $\pm$ 1 $\sigma$
CaO	1.22	1.06	1.21 $\pm$ .11
K <sub>2</sub> O	1.38	1.49	1.55 $\pm$ .14
Na <sub>2</sub> O	.99	1.05	1.10 $\pm$ .09
Fe <sub>2</sub> O <sub>3</sub>	2.05	1.26	1.64 $\pm$ .79
SiO <sub>2</sub>	.89	.63	.96 $\pm$ .55
MgO	3.14	3.01	3.12 $\pm$ .08
TiO <sub>2</sub>	.01	.03	.02 $\pm$ .01
SO <sub>3</sub>	.10	.05	.07 $\pm$ .03
Al <sub>2</sub> O <sub>3</sub>	.44	.27	.35 $\pm$ .10
NiO	.38	.31	.32 $\pm$ .06
ZnO	.09	.07	.07 $\pm$ .02
CoO	.02	.01	.01 $\pm$ .01
CuO	.56	.55	.55 $\pm$ .04
MnO <sub>2</sub>	74.53	75.85	74.91 $\pm$ 1.25
BaO	1.57	1.82	1.51 $\pm$ .22
La <sub>2</sub> O <sub>3</sub>	.00	.00	.00 $\pm$ .00
Ce <sub>2</sub> O <sub>3</sub>	.08	.07	.06 $\pm$ .01
Sm <sub>2</sub> O <sub>3</sub>	.03	.03	.02 $\pm$ .01
P <sub>2</sub> O <sub>5</sub>	<u>.13</u>	<u>.08</u>	.14 $\pm$ .11
Total	87.64	87.64	

Table 5. Continued.

(c) Micro-laminated iron-rich deposit, normalized to 87.64%<sup>(1)</sup>

	#1	#2	#3	#4
CaO	2.19	1.64	1.54	1.81
K <sub>2</sub> O	.25	.63	.28	.25
Na <sub>2</sub> O	.22	.46	.26	.36
Fe <sub>2</sub> O <sub>3</sub>	25.98	14.48	26.43	25.34
SiO <sub>2</sub>	14.55	7.33	16.54	15.37
MgO	2.98	3.93	2.92	2.71
TiO <sub>2</sub>	.13	.20	.24	.11
SO <sub>3</sub>	.13	.09	.05	.18
Al <sub>2</sub> O <sub>3</sub>	1.45	1.28	1.82	1.31
NiO	.45	.77	.24	.45
ZnO	.11	.35	.22	.09
CoO	.13	.16	.11	.04
CuO	.16	.64	.33	.16
MnO <sub>2</sub>	37.69	54.16	35.20	37.30
BaO	.69	.86	.92	1.38
La <sub>2</sub> O <sub>3</sub>	.00	.05	.04	.00
Ce <sub>2</sub> O <sub>3</sub>	.02	.08	.04	.05
Sm <sub>2</sub> O <sub>3</sub>	.03	.12	.07	.07
P <sub>2</sub> O <sub>5</sub>	<u>.45</u>	<u>.38</u>	<u>.37</u>	<u>.63</u>
Total	87.64	87.64	87.64	87.64

(1) These totals were normalized to 87.64% to facilitate comparison with the normalized todorokite compositions.

Table 5. Continued.

(c) Continued

	#5	#6	Mean $\pm$ 1 $\sigma$	Mean $\pm$ 1 $\sigma$ <sup>(2)</sup>
CaO	2.27	2.44	1.98 $\pm$ .37	2.05 $\pm$ .37
K <sub>2</sub> O	.24	.42	.34 $\pm$ .15	.29 $\pm$ .07
Na <sub>2</sub> O	.30	.32	.32 $\pm$ .08	.29 $\pm$ .05
Fe <sub>2</sub> O <sub>3</sub>	23.28	26.00	23.58 $\pm$ 4.59	25.41 $\pm$ 1.25
SiO <sub>2</sub>	14.17	14.94	13.82 $\pm$ 3.28	15.11 $\pm$ .91
MgO	3.00	5.11	3.44 $\pm$ .92	3.34 $\pm$ .99
TiO <sub>2</sub>	.12	.24	.17 $\pm$ .06	.17 $\pm$ .07
SO <sub>3</sub>	.38	.14	.16 $\pm$ .11	.18 $\pm$ .12
Al <sub>2</sub> O <sub>3</sub>	1.47	2.66	1.66 $\pm$ .52	1.74 $\pm$ .55
NiO	.70	1.23	.64 $\pm$ .35	.61 $\pm$ .38
ZnO	.20	.42	.23 $\pm$ .13	.21 $\pm$ .13
CoO	.12	.24	.13 $\pm$ .06	.13 $\pm$ .07
CuO	.30	.10	.28 $\pm$ .20	.21 $\pm$ .10
MnO <sub>2</sub>	39.05	31.85	39.21 $\pm$ 7.74	36.21 $\pm$ 2.81
BaO	1.26	.79	.98 $\pm$ .27	1.01 $\pm$ .30
La <sub>2</sub> O <sub>3</sub>	.00	.04	.02 $\pm$ .02	.02 $\pm$ .02
Ce <sub>2</sub> O <sub>3</sub>	.08	.08	.06 $\pm$ .03	.05 $\pm$ .03
Sm <sub>2</sub> O <sub>3</sub>	.06	.13	.08 $\pm$ .04	.07 $\pm$ .04
P <sub>2</sub> O <sub>5</sub>	<u>.64</u>	<u>.44</u>	.48 $\pm$ .12	.51 $\pm$ .12
Total	87.64	87.64		

(2) Grain #2 excluded.

Table 5. Continued.

(d) Phosphatic fish debris, normalized to 83.03%

	#1	#2	#3	#4	#5	Mean $\pm$ 1 $\sigma$
CaO	44.98	45.86	45.13	44.74	45.19	45.18 $\pm$ .42
K <sub>2</sub> O	.08	.06	.05	.05	.05	.06 $\pm$ .01
Na <sub>2</sub> O	.72	.69	.76	.69	.75	.72 $\pm$ .03
Fe <sub>2</sub> O <sub>3</sub>	.36	.32	.32	.33	.27	.32 $\pm$ .03
SiO <sub>2</sub>	.05	.10	.07	.09	.03	.07 $\pm$ .03
MgO	.60	.64	.64	.86	.68	.68 $\pm$ .10
TiO <sub>2</sub>	.01	.01	.02	.00	.00	.01 $\pm$ .01
SO <sub>3</sub>	.75	.66	.65	.80	.64	.70 $\pm$ .07
Al <sub>2</sub> O <sub>3</sub>	.07	.05	.07	.10	.78	.21 $\pm$ .32
NiO	.00	.00	.00	.00	.00	.00 $\pm$ .00
ZnO	.01	.00	.00	.00	.00	.00 $\pm$ .00
CoO	.00	.00	.00	.00	.00	.00 $\pm$ .00
CuO	.04	.01	.03	.02	.07	.03 $\pm$ .02
MnO <sub>2</sub>	.35	.26	.31	.38	.34	.33 $\pm$ .05
BaO	.00	.00	.00	.00	.00	.00 $\pm$ .00
La <sub>2</sub> O <sub>3</sub>	.24	.24	.28	.35	.26	.27 $\pm$ .05
Ce <sub>2</sub> O <sub>3</sub>	.00	.00	.00	.00	.00	.00 $\pm$ .00
Sm <sub>2</sub> O <sub>3</sub>	.06	.08	.08	.07	.06	.07 $\pm$ .01
P <sub>2</sub> O <sub>5</sub>	<u>34.71</u>	<u>34.09</u>	<u>34.62</u>	<u>34.54</u>	<u>33.91</u>	34.37 $\pm$ .35
Total	83.03	83.03	83.03	83.03	83.03	

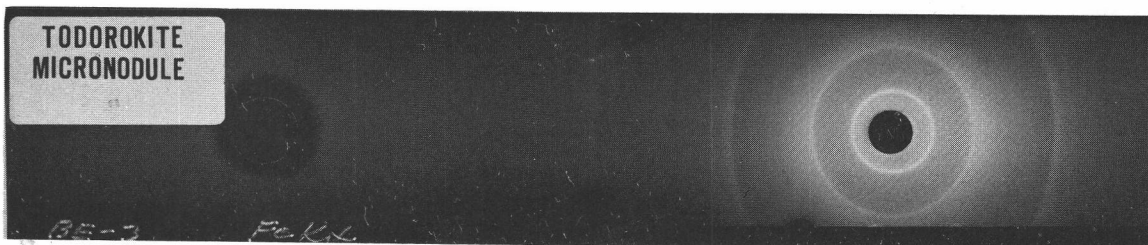
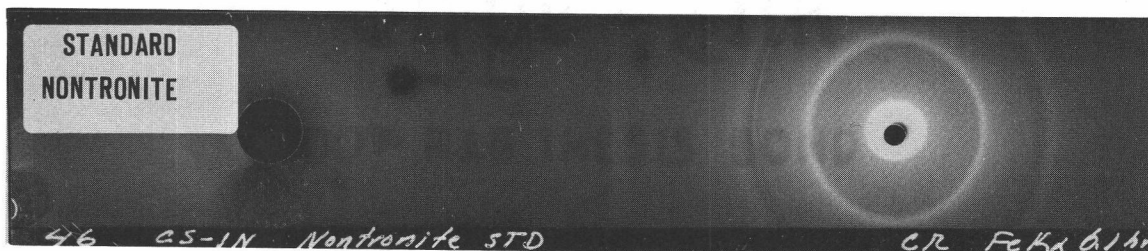
## X-RAY DIFFRACTION ANALYSIS

X-ray diffraction patterns from individual micronodule and smectite grains were obtained using a technique developed for small samples by Dr. R. K. Sorem (1960) (Figure 5). With this technique, grains as small as 10 microns in diameter are mounted on a gelatin fiber in a 57.3 mm diameter Debye-Scherrer diffraction camera. Samples were either hand-picked or scratched from a polished section with a diamond stylus mounted on a micro-manipulator.

A manganese-rich, highly reflective micronodule core taken from a polished section gave a diffraction pattern (Figure 5) identical to that of todorokite from Charco Redondo, Cuba (Straczek et al., 1960). No extraneous diffraction lines were noted. The unusually high quality of the diffraction pattern may be attributed to the sample preparation. Since whole fragments were mounted in the X-ray camera, grinding the sample was unnecessary. Grinding manganese oxides has been shown by Burns and Brown (1972) to result in poor diffraction patterns because of damage to the crystalline structure. Whole micronodules hand-picked from coarse fraction separates also gave todorokite patterns with no extraneous lines assignable to other minerals.

Hand-picked lemon-yellow smectite aggregates gave excellent diffraction patterns (Figure 5), but the similarity of the standard

Figure 5. X-ray diffraction patterns. All patterns obtained using a 57.3 mm diameter Debye-Scherrer camera with Fe radiation.



nontronite and montmorillonite patterns does not allow distinction of these phases in untreated samples. No extraneous peaks were present. The diffuseness of the Bauer Deep smectite pattern may be the result of small crystallite sizes.

## DISCUSSION

### Smectites

The oxide weight percent totals for the smectite grains range from 67 to 95 percent (Table 4a). Both the SEM photographs and the analytical results suggest that the cause of the spread in the oxide weight totals is variable and often high porosity rather than poor or incomplete analyses. The delicate intergrowth of bladed smectite crystals depicted in the SEM photographs supports the suggestion of high porosity. Such a structure, when analyzed with a wide (20 micrometer) electron beam would give a low oxide weight total, but with the relative elemental concentrations unchanged.

When the analytical results are normalized to conform with the highest oxide total obtained (94.9%), the variation in elemental oxide concentrations among the eleven grains is small (Table 5a), suggesting that the variation in the raw oxide totals is caused by variations in porosity or water content rather than by variations in relative composition.

The results were normalized to the highest total obtained because this analysis is assumed to represent a lower limit to the amount of porosity present. Since it is impossible to determine the relative contributions of structural water and porosity to the low totals, the highest total obtained is taken to represent a 'porosity-free' analysis. Since the amount of water lost on ignition by smectites is typically 5-10% (Ross and Hendricks, 1945), the value of 94.9% to which all the smectite analyses have been normalized (Table 5a) is probably a good estimate of the absolute composition. It follows that the upper limit of the structural water content of these smectite grains is 5.1 percent.

Variations in composition among the eleven grains analyzed appears to be mostly caused by contamination with varying amounts of intergranular iron and manganese oxides. Grain #10 (Table 5a) shows enrichment in Fe, Mn, Ni, Ca, and Na, and depletion of Si, Al, Mg, and K, relative to the other smectite grains. Each of the former elements are also enriched in the todorokite or iron-rich phase (Table 5b and 5c) relative to the smectite, whereas the latter elements are also depleted in the ferromanganese phases relative to the smectite. This apparent covariation between those elements which appear in the ferromanganese phases and those elements which appear as contaminants in the smectite suggests that the variations in the compositions of the smectite grains are largely caused by

admixture of ferromanganese impurities, rather than poor analyses or natural variation in the smectite composition. Figure 6 also shows that the deviation of one or two grains from the other analyses is toward higher iron and manganese compositions. The most anomalous analysis (grain #10) was deleted from the calculation of the mean smectite composition (Table 5a). Deletion of grain #10 reduces the standard deviation of each of the elements listed above.

The chemical compositions of the smectite grains have been recalculated to molar proportions and fitted to the general smectite composition  $Y_{4-6}Zr_8O_{20}(OH)_4 \cdot nH_2O$  (MacEwan, 1961). Ca, Na, K, and Ba are assumed to be interlayer cations. The equivalent concentrations of these elements were used to calculate the interlayer charge. Molar proportions were adjusted to give a total unit cell with 44 equivalents. All iron is assumed to be in the Fe(III) state because of the oxidized state of the core and the lemon-yellow color of the smectite grains. Net unit cell charges were forced to balance the interlayer cation charge by transfer of  $Al^{+3}$  and  $Fe^{+3}$  into the tetrahedral layer as necessary. On the basis of ionic radii considerations,  $Al^{+3}$  was assigned to the tetrahedral layer until it either satisfied the charge balance requirements or was exhausted. Iron was assigned to the tetrahedral layer as was necessary only after exhaustion of all the available aluminum.

Although this preferential assignment of  $Al^{+3}$  over  $Fe^{+3}$  to the

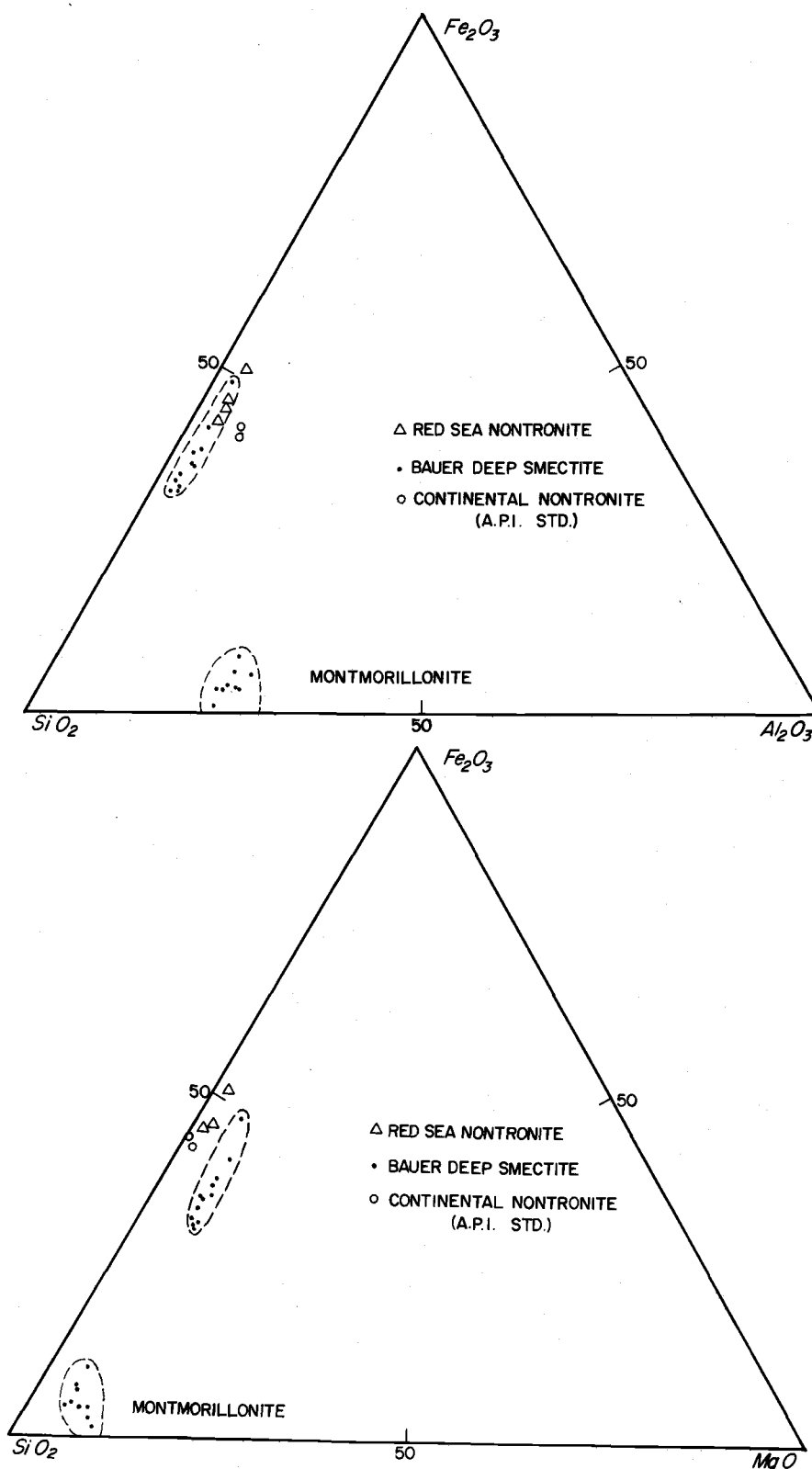


Figure 6. Comparison of major element concentrations in Bauer Deep smectites, Red Sea nontronites (Bischoff, 1972), standard continental nontronites (Kerr *et al.*, 1951), and standard montmorillonites (Kerr *et al.*, 1951).

tetrahedral layer is on a sound basis with respect to ionic radii considerations and has been used previously (cf. Bischoff, 1972), it should be noted that there are no structural data to support such a procedure in the case of the Bauer Deep smectites. Osthaus (1954) used acid dissolution techniques to suggest that a nontronite sample contained considerable iron in addition to aluminum in tetrahedral coordination, despite the fact that enough aluminum was present to compensate for the silicon deficiency. Considerable amounts of aluminum and iron were present in both the tetrahedral and octahedral layers. Hence, although aluminum has been assigned preferentially to the tetrahedral layer in this study because no structural determinations have been made, the resulting iron and aluminum distributions must be considered tentative.

It should also be noted that phosphorous and sulfur have been assigned to octahedral positions. This assignment is arbitrary, but in any event the concentrations are so small that the structural picture is not affected.

The calculated structures from each analysis as well as a 'mean' structure determined from the mean molar composition are presented in Table 6. It is evident that the compositions indeed fit a smectite structure. Net unit cell charges range from 0.60 to 0.88 and for each analysis the sum of the octahedral cations falls within the theoretical mole range of 4-6. The 'average' smectite gives a

Table 6. Distribution of Cations Per Lattice Unit in Smectite.

		#1	#2	#3	#4
	Si <sup>+4</sup>	7.370	7.361	7.172	7.620
Tetrahedral	Al <sup>+3</sup>	.456	.476	.411	.380
	Fe <sup>+3</sup>	.174	.163	.416	.000
<u>Tet. Cations</u>		<u>8.000</u>	<u>8.000</u>	<u>8.000</u>	<u>8.000</u>
	Fe <sup>+3</sup>	3.074	3.106	2.905	2.821
	Al <sup>+3</sup>	.000	.000	.000	.080
	Mg <sup>+2</sup>	1.211	1.122	1.333	1.333
	Mn <sup>+4</sup>	.037	.067	.119	.052
	Ni <sup>+2</sup>	.006	.008	.000	.018
Octahedral	Zn <sup>+2</sup>	.010	.005	.000	.002
	Co <sup>+2</sup>	.006	.005	.000	.004
	Cu <sup>+2</sup>	.015	.009	.006	.010
	Ti <sup>+4</sup>	.003	.005	.006	.002
	S <sup>+6</sup>	.005	.006	.006	.009
	P <sup>+5</sup>	.009	.015	.030	.015
<u>Oct. Cations</u>		<u>4.376</u>	<u>4.348</u>	<u>4.405</u>	<u>4.346</u>
	Ca <sup>+2</sup>	.061	.059	.111	.040
Interlayer	K <sup>+1</sup>	.355	.382	.377	.392
	Na <sup>+1</sup>	.193	.123	.141	.119
	Ba <sup>+2</sup>	.001	.001	.000	.003
<u>Interlayer charge<sup>(1)</sup></u>		<u>.672</u>	<u>.625</u>	<u>.740</u>	<u>.597</u>

(1) In equivalents per unit cell.

Table 6. Continued.

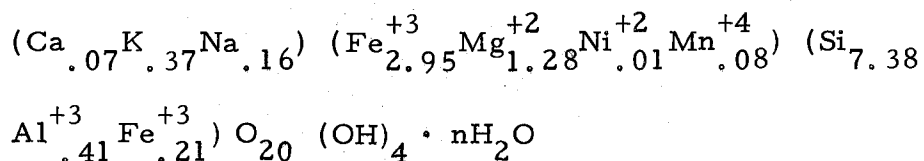
	#5	#6	#7	#8
Si <sup>+4</sup>	7.120	7.539	7.581	7.520
Tetrahedral Al <sup>+3</sup>	.452	.319	.418	.342
Fe <sup>+3</sup>	.428	.141	.000	.138
<b>Tet. Cations</b>	<b>8.000</b>	<b>8.000</b>	<b>8.000</b>	<b>8.000</b>
Fe <sup>+3</sup>	3.015	2.805	2.917	2.946
Al <sup>+3</sup>	.000	.000	.018	.000
Mg <sup>+2</sup>	1.264	1.398	1.207	1.275
Mn <sup>+4</sup>	.100	.103	.070	.057
Ni <sup>+2</sup>	.014	.015	.017	.019
Octahedral Zn <sup>+2</sup>	.000	.000	.000	.002
Co <sup>+2</sup>	.000	.000	.002	.005
Cu <sup>+2</sup>	.000	.000	.003	.009
Ti <sup>+4</sup>	.004	.000	.002	.003
S <sup>+6</sup>	.004	.005	.008	.009
P <sup>+5</sup>	.027	.013	.025	.018
<b>Oct. Cations</b>	<b>4.428</b>	<b>4.339</b>	<b>4.269</b>	<b>4.343</b>
Ca <sup>+2</sup>	.093	.071	.056	.068
Interlayer K <sup>+1</sup>	.375	.372	.378	.329
Na <sup>+1</sup>	.141	.204	.204	.194
Ba <sup>+2</sup>	.000	.000	.003	.004
<b>Interlayer charge</b>	<b>.703</b>	<b>.718</b>	<b>.699</b>	<b>.665</b>

Table 6. Continued.

	#9	#10	#11	Mean $\pm 1\sigma$ <sup>(2)</sup>	
	Si <sup>+4</sup>	7.700	6.291	6.903	7.388 $\pm$ .254
Tetrahedral	Al <sup>+3</sup>	.300	.353	.362	.406 $\pm$ .060
	Fe <sup>+3</sup>	.000	1.356	.735	.206 $\pm$ .238
<hr/>					
Tet. Cations					
	Fe <sup>+3</sup>	2.808	3.157	.056	2.954 $\pm$ .113
	Al <sup>+3</sup>	.048	.000	.000	.000
	Mg <sup>+2</sup>	1.399	.999	1.331	1.285 $\pm$ .142
	Mn <sup>+4</sup>	.061	.215	.098	.077 $\pm$ .036
	Ni <sup>+2</sup>	.013	.022	.010	.013 $\pm$ .005
Octahedral	Zn <sup>+2</sup>	.000	.000	.000	.002 $\pm$ .000
	Co <sup>+2</sup>	.000	.004	.000	.002 $\pm$ .000
	Cu <sup>+2</sup>	.003	.007	.000	.006 $\pm$ .004
	Ti <sup>+4</sup>	.000	.013	.005	.003 $\pm$ .002
	S <sup>+6</sup>	.011	.008	.003	.006 $\pm$ .002
	P <sup>+5</sup>	.031	.066	.024	.020 $\pm$ .007
<hr/>					
Oct. Cations					
	Ca <sup>+2</sup>	.069	.148	.085	.071 $\pm$ .020
Interlayer	K <sup>+1</sup>	.376	.287	.350	.368 $\pm$ .018
	Na <sup>+1</sup>	.158	.294	.172	.164 $\pm$ .032
	Ba <sup>+2</sup>	.006	.001	.000	.002 $\pm$ .001
<hr/>					
Interlayer charge					
		.684	.878	.693	.678 $\pm$ .042

(2) Calculated from mean molar composition.

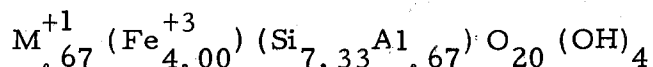
composition corresponding to the formula:



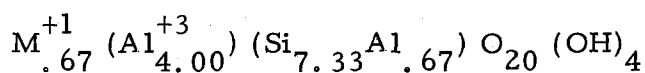
The relative proportions of the four major elements (Si, Fe, Al, and Mg) have been plotted in Figure 6 to show the general relationship between the composition of these Bauer Deep smectites and both nontronites and montmorillonites. In Figure 6 the continental nontronites and montmorillonites presented are American Petroleum Institute standard clay minerals (Kerr *et al.*, 1951).

The structural formula given above places the Bauer Deep smectites within the structural and chemical boundaries of a nontronite. End members of the continuous nontronite-beidellite series are (MacEwan, 1961):

Nontronite



Beidellite



Based on these ideal compositions, the Bauer Deep nontronite is distinguished by its high iron and magnesium contents. The substitution of iron for aluminum in the tetrahedral positions characterizes the Bauer Deep nontronite as slightly more iron-rich than the

nontronite end member of the ideal nontronite-beidellite series. The general chemical similarities between the Bauer Deep nontronite and both continental and Red Sea nontronites are evident in Figure 6.

The high magnesium content of the Bauer Deep nontronite is unusual in that the results of Ross and Hendricks (1945) suggest that high-iron smectites are usually low in magnesium. Both continental nontronites and Red Sea nontronites contain less than half as much magnesium as the Bauer Deep nontronites (Figure 6). Although the Bauer Deep nontronite and the Red Sea nontronite are generally similar, they are distinguished by the relatively large amounts of Cu and Zn and the lesser amount of magnesium in the Red Sea nontronite (Bischoff, 1972). The Red Sea nontronite also appears to be distinguished by the presence of ferrous iron in the octahedral layer.

This occurrence of nontronite in the Bauer Deep establishes the formation of an authigenic smectite species in pelagic metalliferous sediment. As such, it raises the question as to what extent this process occurs in more typical pelagic sediments. Further work is required to determine whether this authigenic precipitation of nontronite is unique to deposits of metalliferous sediment in volcanically active regions or whether it is a more widespread phenomenon which is normally obscured by terrigenous, eolian, or biogenous sedimentation.

A persistent problem in the analysis of clay minerals is the

presence of contaminants. In this case, the question as to whether or not there are large amounts of iron-rich impurities in the nontronite aggregates strongly affects the determination of the mineral species. As noted above, the X-ray diffraction patterns are only sufficient to establish the unequivocal presence of either montmorillonite or nontronite. However, it is also to be noted that there are no other crystalline species present in the Bauer Deep smectite aggregates, suggesting that any impurities present are amorphous. Although the presence of small amounts of amorphous iron-bearing impurities cannot be conclusively ruled out, previous analyses of both Red Sea nontronites and fine-grained smectites from the East Pacific Rise suggest that the Bauer Deep nontronites analyzed in this study are not substantially contaminated. The Red Sea nontronites analyzed by Bischoff (1972) contain higher Fe-Si ratios after dithionite-citrate treatment (Mehra and Jackson, 1958) for removal of iron oxides than do the Bauer Deep nontronites of this study (Figure 6). In addition, partial analyses of dithionite-treated clay fractions of metalliferous sediment from the East Pacific Rise by John Kendrick and Dave Rea (1972, written communication) also indicate high iron concentrations. Finally, optical examination, as noted above, reveals no evidence of iron-bearing impurities.

### Micronodules

The quantitative results (Tables 4 and 5) confirm the presence of two chemically distinct ferromanganese phases comprising the micronodules of sample AII 54-14. The structure, chemistry, and morphology of these phases are all related to the origin of the micronodules and may reflect on the origin of the sediment.

(a) Morphology. As noted in Table 3, 90 percent of the 412 micronodules examined in polished section exhibit either an apparently homogeneous (micro-laminated) structure or a two-phase structure with a consistent sequence of deposition of the two types of phases. The predominance of these two structures may be explained in two ways, both of which are consistent with a single model for the origin of the micronodules.

If most of the micronodules are composed of a massive todorokite core surrounded by an iron-rich rind, a collection of random cross sections of micronodules would be expected to exhibit the observed morphologies. That is, the apparent presence of two morphologies may be an artifact caused by the random mounting and polishing technique. The random distribution of micronodules in the epoxy matrix would cause some of the micronodules to be cut and polished on a plane passing through only the outer, iron-rich rind, and others on a plane through both phases. Since the relative sizes

of the core and rind are highly variable it is impossible to speculate as to the theoretical distribution of cross section types in such a case.

Alternatively, distinct structures may be present; micronodules comprised solely of the iron-rich micro-laminated deposit and micronodules comprised of a todorokite core and iron-rich rind.

In either case, the formation of the micronodules may be inferred to have proceeded in two stages -- a period of deposition of todorokite followed by a period of deposition of the iron-rich, micro-laminated material. Such a model would account for the presence of exclusively two-phase micronodules, each micronodule reflecting both periods of deposition, as well as the presence of a combination of one- and two-phase micronodules. The rarer occurrence of other observed structures might be ascribed to partial sediment reworking and consequent introduction of micronodules with different depositional histories.

Another hypothesis which should be considered is alteration of todorokite micronodules by sea water to give an alteration rind. Manganese mobilization at depth might include partial dissolution and alteration of micronodules, resulting in concentric rinds around unaltered cores. However, the quantitative analyses argue against this, since the compositions would require transfer of large amounts of silicon and iron into the micronodule to replace the dissolved manganese. Additionally, the micro-laminations in the rind material are

characteristic of typical concretionary deposits, rather than alteration products.

The fact that almost all the micronodules in a sample developed in the same way (todorokite followed by a micro-laminated phase) has important consequences for the history of authigenic mineral precipitation within the sediment. It implies that the micro-environment from which the ferromanganese deposits precipitated changed at some time such that deposition of todorokite ceased and deposition of a micro-laminated phase or phases commenced. This model of a systematic change in mineralogy contrasts with the alternative model random nucleation or epitactic crystallization of one mineral upon another. The depositional sequence in the micronodules implies that whatever changes occurred in the micro-environment of the sediment to cause the changes in authigenic precipitation are recorded in the morphology of the micronodules.

Although the morphologies of micronodules have not been studied previously, studies of larger nodules (Sorem and Foster, 1972) has shown similar correlations of depositional histories among nodules recovered from a single dredge haul, as well as among nodules from different dredge hauls taken close together. The relatively simple structures of micronodules as compared to macronodules should facilitate more conclusive stratigraphic studies, since correlation of the hundreds or thousands of layers of variable thickness within

macronodules is quite difficult. In addition, the detailed correlation of depositional sequences within surficial macronodules reflects the history of ferromanganese deposition during the lifetime of the nodule, whereas the analysis of depositional sequences in micronodules from any point in an oxidized sediment column should provide a history of ferromanganese deposition during the time that authigenic precipitation took place in the sediment.

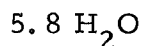
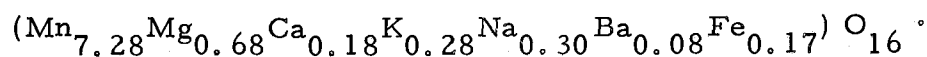
(b) Mineralogy-Todorokite. The todorokite cores are essentially monomineralic except for micro-inclusions of unidentified contaminants. Quantitative analyses (Table 4b) gives consistently high (85-87%) oxide weight totals which are within the range expected when structural water is taken into account. The high reflectivity of the polished samples and their radial anisotropy suggest a relatively dense, crystalline structure. The fine-grained ( $< 1\mu\text{m}$ ) nature of the todorokite is indicated by the size of the radially anisotropic crystallites. The todorokite is exceptionally stable under the electron beam of the microprobe, showing no tendency to deteriorate even after long periods of exposure. The high analytical totals also indicate that the porosity of the todorokite approaches the porosity of the standards, all of which are essentially non-porous glasses, minerals, or pure metals.

This occurrence of todorokite as a highly reflective,

anisotropic deposit is similar to occurrences of todorokite in macronodules. Sorem and Foster (1972) have identified both birnessite and todorokite in massive, highly reflective laminae of manganese nodules, and Andruschenko and Skornyakova (1969) report psilomelane and todorokite in the form of small, highly reflective globules comprising manganese nodules. This identification of todorokite in the deep water (4200 m) deposit studied here is also consistent with the common occurrence of todorokite in deep pelagic nodules (Barnes, 1967; Cronan and Tooms, 1969).

The major element composition of the todorokite (Table 5b) is similar to published analyses of continental deposits of todorokite (Frondel et al., 1960). Minor element concentrations are similar except that the micronodule todorokite is relatively enriched in copper and nickel, and apparently enriched in iron, although the iron enrichment may be caused by admixture of iron-rich micro-inclusions.

In order to calculate an approximate formula for the todorokite, the mean composition (Table 5b) has been recast in atomic proportions. If the deficiency in the oxide weight total is assigned to structural water, the formula is:



(c) Mineralogy-Micro-laminated Rind. The micro-laminated rind is both structurally and mineralogically unlike the todorokite. As noted above, microscopic examination reveals concentric micro-laminae of unidentifiable components. Similar micro-laminae in micronodules have been observed by scanning electron microscopy (Margolis, 1973). The characteristically poor reflectivity, apparent isotropism, and tendency to deteriorate slowly under the electron beam indicate a structure different from the dense, massive todorokite. The quantitative analyses give low and highly variable oxide weight totals (39-65%, Table 4c), which can be attributed to the highly porous structure visible in the SEM photographs. Both the instability under the electron beam and the low analytical totals are probably caused by the high porosity. High porosity results in poor heat conduction - the primary cause of deterioration under an electron beam. Because porosity leads to a proportional reduction in the apparent concentration of all elements, all analyses of the rind material have been normalized to give a total oxide weight equal to that of the todorokite analyses (Table 5c) so as to facilitate comparison of analyses of the two phases. This procedure also brings the totals up to a value close to those for typical nodules.

The analytical data suggest that the iron-rich rind consists of several minerals. Both the variability of major element abundances in the six analyses and the actual major elements identified suggest

that at least three phases are present. This is shown more clearly in Figure 7 which compares the proportions of  $\text{MnO}_2$ ,  $\text{SiO}_2$  and  $\text{Fe}_2\text{O}_3$  in the rind material to their proportions in the todorokite and nontronite from this study and in typical manganese nodules. The following observations can be made from this figure:

- (1) Rind material does not appear to be a simple mixture of todorokite and nontronite. Connection of the todorokite and nontronite composition fields shows that excess iron is present in the rind material. The absence of identifiable minerals, other than todorokite, in the X-ray diffraction patterns of whole micronodules suggests that the excess iron is amorphous.
- (2) Furthermore, most of the manganese nodules presented in Figure 7 also fall above the todorokite-nontronite tieline, implying that excess iron oxide species are present in most manganese nodules. The high silicon content of nodules falling below the tieline may be caused by detrital contamination.
- (3) The micro-laminated, iron-rich material from the Bauer Deep has a major element composition similar to macro-nodules from the Pacific.
- (4) The bulk sediment composition falls on a tieline connecting the fields of rind material and nontronite. Thus, the

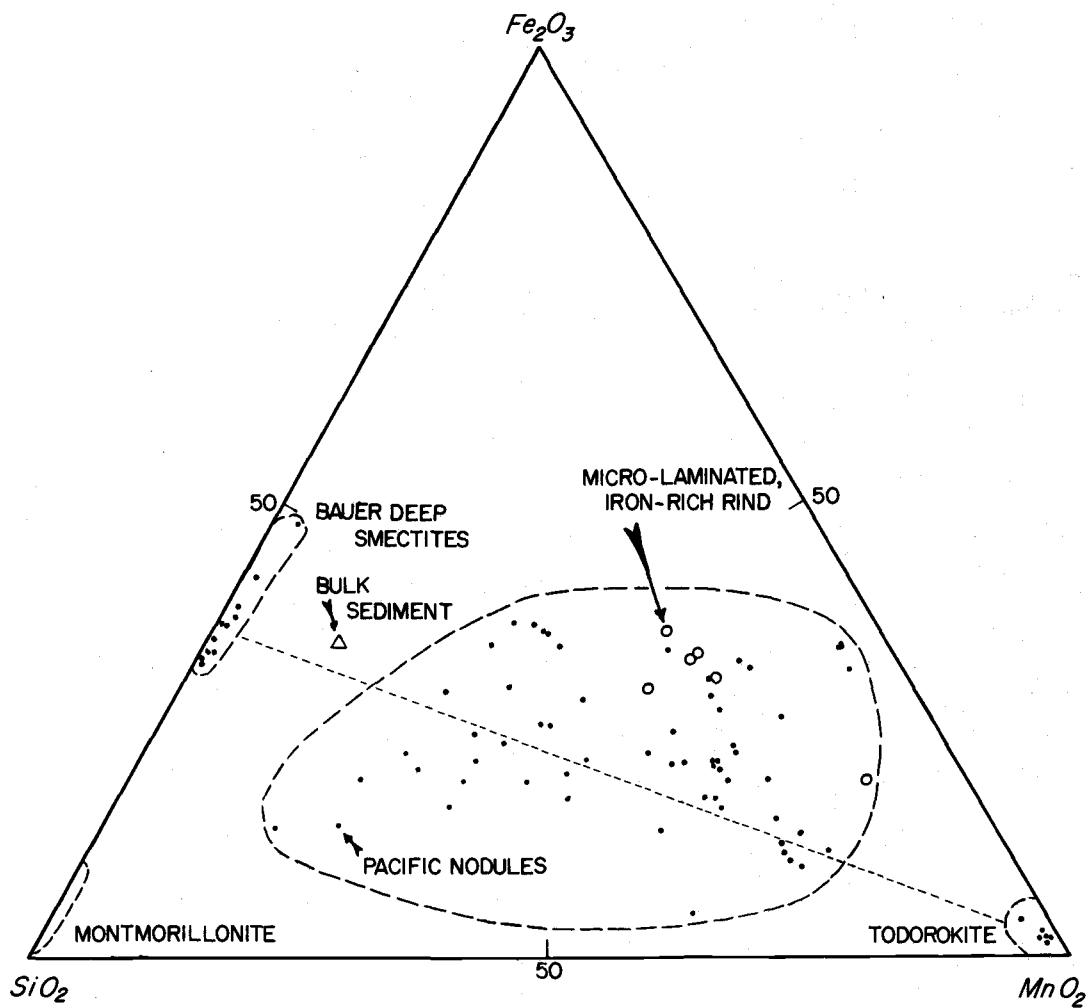


Figure 7. Major element relationships of todorokite, iron-rich rind, smectite, and typical North Pacific manganese nodules. Dashed line encloses range of values for North Pacific nodules. Data for North Pacific nodules are from Horn *et al.* (1972).

composition of the bulk sediment can be accounted for by these two species.

Thus, the composition of the rind material can be interpreted as a mixture of todorokite, nontronite of the composition measured in this study, and an amorphous iron hydroxyoxide. Alternatively, a simple mixture of a high iron nontronite or an unknown iron-manganese-silicate mineral could account for the observed rind composition. Since I did not measure any smectites which would fall in the extremely high-iron class and the presence of an iron-manganese-silicate mineral has never been described in marine sediments, the first explanation seems preferable. Additionally, a nontronite with a higher concentration of iron than that measured in this study is unlikely because of the limited capacity of the smectite structure to accept iron substituting for silicon.

(d) Chemistry. Figure 8 shows the abundance patterns of selected elements in the todorokite and the micro-laminated rind material. Of the transition metals, iron, nickel, zinc, and cobalt are concentrated in the rind material, whereas copper is more abundant in the todorokite. Cobalt is clearly concentrated within the iron-rich phases of the micronodules relative to the manganese-rich phases (Figure 8). This supports the conclusions of Burns and Fuerstenau (1966) and Burns and Brown (1972) based on qualitative

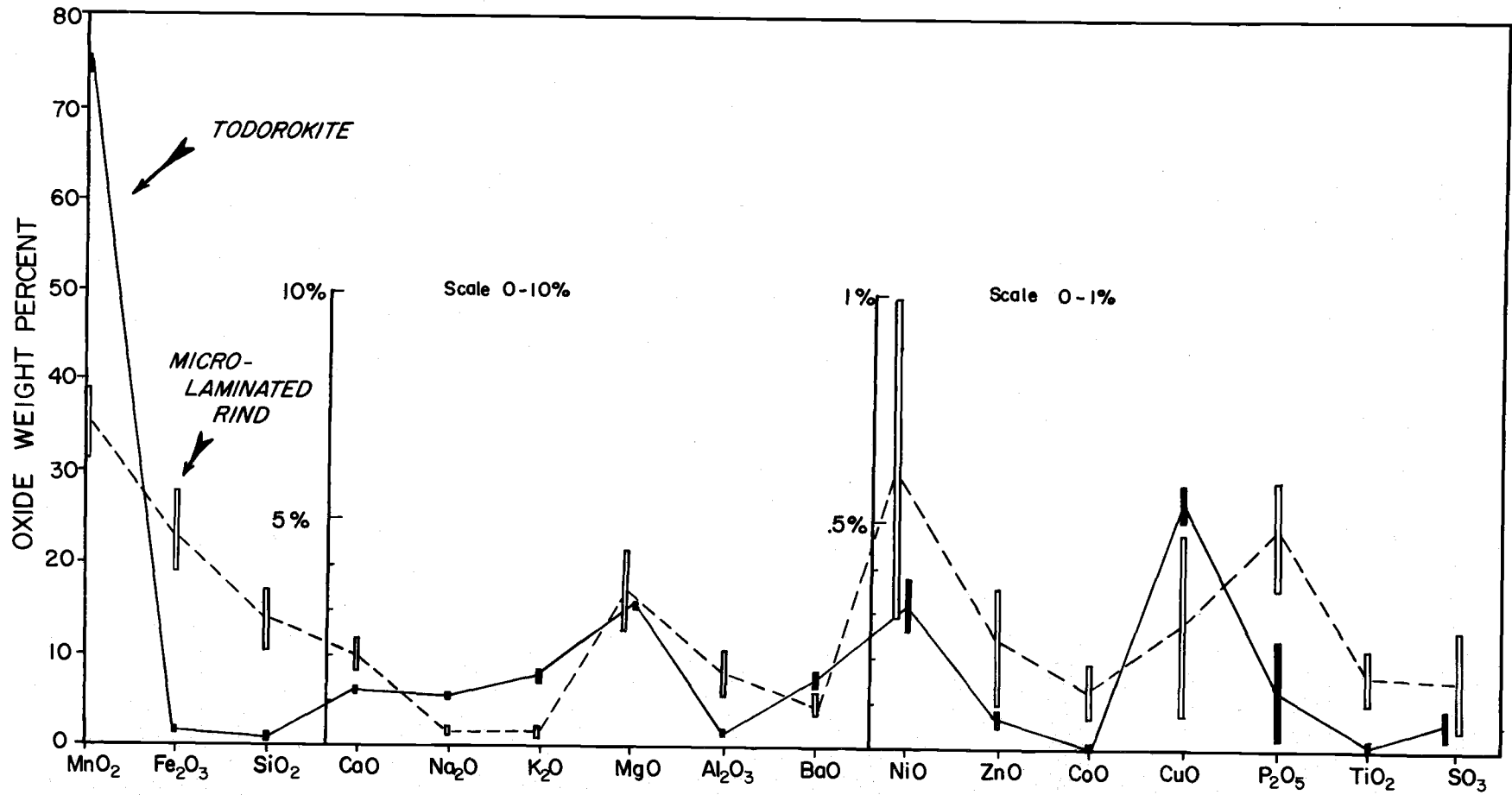


Figure 8. Element distributions in todorokite and iron-rich rinds. Lengths of error bars are  $2\sigma$ .

microprobe traverses of nodules, and of Goldberg (1954) and Riley and Sinhaseni (1958) based on bulk analyses of nodules. The observed covariance of cobalt and iron in these micronodules is consistent with the suggestion of Burns (1965), based on theoretical considerations, that isomorphous substitution of Co(III) for Fe(III) in iron oxides is feasible in oxidizing marine environments where additional Co(II) is added to sea water by volcanic input. In contrast, the higher concentration of nickel in the rind conflicts with the results obtained by Burns and Brown (1972), who found covariance of Ni and Mn concentrations in microprobe traverses of manganese nodules.

Barium in the sediment occurs primarily in the two ferromanganese phases and in barite. The higher concentration of barium in the todorokite relative to the Fe-rich phase apparently reflects the preferential coprecipitation of barium and manganese. Thus, barium concentrations (as BaO) range from .00 to 4.32% in todorokites (FrondeLL et al., 1960), and Bonatti et al. (1972) have observed a covariation of Ba and Mn in hydrothermal Fe-Mn deposits. Although the presence of barite is confirmed by X-ray diffraction of the bulk sediment, little or no barite is observed in the coarse fraction. Since barium is more concentrated in the bulk sediment (3.10% as BaO) than in any of the coarse grains analyzed, most of the barium must be present as fine-grained barite. The absence of coarse euhedral grains of barite characteristic of many pelagic

biogenous sediments in the Bauer Deep sediment may suggest that there is a difference in the origins of the barite in sediments that is reflected in the grain size. Barium introduced into sea water hydrothermally may coprecipitate with ferromanganese oxides or precipitate rapidly with sea water sulphate to form fine-grained barite, whereas Barium introduced and concentrated in pelagic sediments by biogenous fallout (Church, 1970) may precipitate slowly to produce large euhedral barite crystals.

Phosphorus is several times more concentrated in the iron-rich phases of the micronodules than in either the todorokite or the silicate grains. This is direct evidence in support of the suggestion by Berner (1973) that dissolved sea water phosphate is preferentially absorbed by poorly crystallized hydrous ferric oxides.

Sulfur is concentrated in the phosphatic fish debris by almost a factor of ten relative to the other phases analyzed (Table 5d). Since this sulfur undoubtedly is derived from sea water, the concentration of sulfur in the fish debris may partially account for the observed  $S^{34}/S^{32}$  ratio of the bulk sediment (Dymond et al., 1973). Even though fish debris constitutes only two percent of the coarse fraction, the concentration of sulfur with a  $S^{34}/S^{32}$  ratio equal to that of sea water in the fish debris may largely determine the  $S^{34}/S^{32}$  ratio of the bulk sediment.

(e) Rare Earth Element Distributions. Because of the low concentration of rare earth elements (REE) in the samples and the lower intensity of the  $L_{\alpha}$  X-ray lines used for analysis, the analytical results are subject to relatively large uncertainties. However, although the absolute concentrations are in some cases questionable, the observable trends appear capable of testing previous contentions based solely on bulk analyses (Dymond et al., 1973).

Of the REE, lanthanum, cerium, and samarium were chosen for analysis in order to investigate both overall REE concentrations within the various phases and the relative enrichment or depletion of cerium in each of the phases.

La, Ce, and Sm are below the detection limit ( $< 100$  ppm) in each of the nontronite grains analyzed. As expected, the large ionic radii of the REE apparently preclude their substitution in either the tetrahedral or octahedral lattice sites of the nontronite structure. Even though nontronite is the most abundant component of the sediment, the low concentration of REE in this phase suggests that the bulk sediment REE distribution may be largely determined by the much higher concentrations of REE in the ferromanganese and biogenous phosphate phases.

Figure 9 shows the lanthanum and cerium concentrations in the todorokite, phosphatic fish debris, and micro-laminated, iron-rich phases. For comparison, the La and Ce concentrations

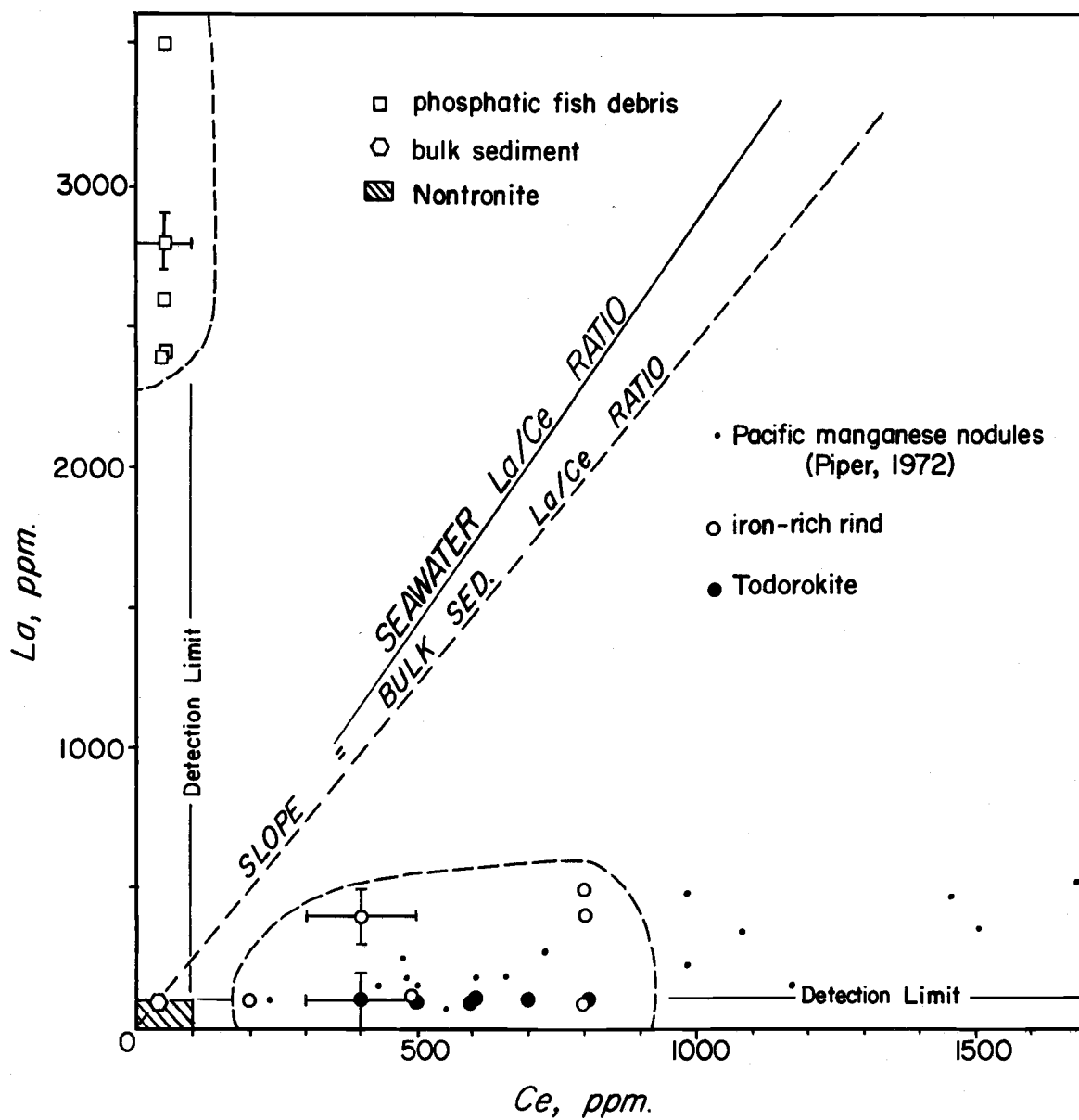


Figure 9. La and Ce concentrations. Representative error bars are  $2\sigma$  for counting statistics only.

of a number of Pacific manganese nodules (Piper, 1972) have also been plotted. The La and Ce concentrations of the bulk sediment (Dymond et al., 1973) are also plotted as are lines representing the La/Ce ratios of the sea water and the bulk sediment.

Both the todorokite and the micro-laminated iron-rich deposits have the relatively high Ce concentration characteristic of ferromanganese nodules. The concentration of lanthanum was below the detection limit in all the todorokite analyses and in three of the six rind analyses.

The phosphatic fish debris contains high (2400-3500 ppm) concentrations of La but undetectable amounts of Ce. The concentrations of both La and Sm in this phase agree well with the values presented for fish bone apatite by Arrhenius and Bonatti (1965), but the Ce concentration is lower than their value by a factor of ten.

Taken together, the La-enriched phosphatic fish debris and the Ce-enriched ferromanganese phases could account for the bulk sediment La/Ce ratio. Dilution of these phases by the nontronite can account for the low total REE concentration of the bulk sediment as well as the La/Ce ratio. Hence, the similarity of the bulk sediment REE distribution to the sea water REE distribution may simply reflect a particular mixture of ferromanganese grains and phosphatic fish debris rather than the dominant influence of sea water in controlling the composition of the metalliferous sediments (cf. Bender

et al., 1972).

## CONCLUSIONS

1. The internal morphology and micro-stratigraphy of manganese micronodules provide a more consistent and interpretable history of ferromanganese precipitation from sea water than do surficial macronodules. The uniform stratigraphy of micronodules from a single sediment sample implies that changes in the chemical micro-environment of the sediment control mineral phases precipitated from sea water. This line of reasoning leads to the conclusion that:

(a) Well-preserved micronodules from a sediment sample contain a record of ferromanganese deposition which can be determined and interpreted with standard micro-analytical tools.

(b) Variations in this recorded depositional history has the potential to augment standard biostratigraphic methods of correlation, provided that such variations correspond to widespread variations in the chemical conditions prevailing at the sea floor.

2. The nontronite present Bauer Deep sediments is characterized by high Fe/Si ratios and very low Al concentrations. The high Fe concentration in this phase and the relative abundance of nontronite in the coarse fraction of the sediment indicate that a large percentage of the total iron content of metalliferous sediment is contained in this

phase. The nontronite analyzed in this study has a chemical composition generally similar to nontronite described in the metal-bearing sediments underlying the hot brines of the Red Sea (Bischoff, 1972), but is distinguished by a higher magnesium content.

This occurrence of nontronite establishes it as an authigenic component of metalliferous sediment from the Bauer Deep. Its composition is unlike those of other smectites formed in the oceans as a result of low temperature weathering and unlike continental montmorillonites. This suggests that formation of the Bauer Deep nontronite is either linked to hydrothermal processes which have been suggested to occur at the spreading centers of the world, or is a simple authigenic precipitation which is dominant in the Bauer Deep because of the lack of dilution by terrigenous input.

3. The existence of authigenic nontronite and todorokite in metalliferous sediment indicates that these components precipitated from sea water under similar conditions. Because they presumably crystallized from the same sea water solution, it may be inferred that they represent crystalline phases in thermodynamic equilibrium.

4. The bulk chemistry of the micronodules suggests that they are comprised of at least three phases, two of which are todorokite and an iron oxide species. Although the mineralogy and chemistry of the third phase is not definitely established, the association of the micronodules with discrete aggregates of authigenic nontronite

suggests that nontronite is the third phase.

5. The mineralogy, bulk chemistry, and REE distribution in manganese micronodules from the Bauer Deep do not differ from manganese nodules from other parts of the sea floor. This seems to suggest that both micronodules and macronodules form by the same process.

6. The major element composition of the bulk sediment can be adequately accounted for by a mixture of nontronite and the iron-rich micro-laminated phase. This suggests that the nontronite and micro-nodule phases which are most abundant in the coarse fraction of the sediment are also the major components of the bulk sediments.

7. The La/Ce ratios in ferromanganese micronodules and phosphatic fish debris from metalliferous sediment are similar to La/Ce ratios in the same phases from other marine sediments. The REE distribution in bulk metalliferous sediment is probably determined by the relative proportions of the ferromanganese and phosphatic components, and only coincidentally resembles the sea water distribution in the AII 54-14 sample from the Bauer Deep.

8. Finally, and most importantly, none of the conclusions reached in this study require a model of hydrothermal activity to account for the phases studied. The bulk sediment chemistry can be accounted for by the compositions of the nontronite and the micronodules. The chemistry, mineralogy, and REE distribution of the

micronodules resemble the properties of typical oceanic manganese nodules. The unusual REE distribution of the bulk sediment can be interpreted to be the result of an unusual combination or otherwise normal components. The authigenic nontronite may be a widespread occurrence which is diluted and masked by terrigenous or biogenous sedimentation in other marine environments.

## BIBLIOGRAPHY

- Andrushchenko, P. F. and Skornyakova, N. S., 1969, The textures and mineral composition of iron-manganese concretions from the southern part of the Pacific Ocean. *Oceanology*, v. 9(2), p. 229-242.
- Arrhenius, G. and Bonatti, E., 1965, Neptunism and vulcanism in the ocean. In Mary Sears (ed.), *Progress in oceanography*, v. 3, Pergamon Press Ltd, p. 7-23.
- Barnes, S., 1967, Minor element composition of ferromanganese nodules. *Science*, v. 157(3784), p. 63-65.
- Bender, M., Broecker, W., Gornitz, V., Middel, V., Kay, R., Sun, S. and Biscaye, P., 1971, Geochemistry of three cores from the East Pacific Rise. *Earth Planet. Sci. Lett.*, v. 12, p. 425-433.
- Berner, R. A., 1973, Phosphate removal from sea water by adsorption on volcanogenic ferric oxides. *Earth Planet. Sci. Lett.*, v. 18, p. 77-86.
- Bischoff, J. L., 1972, A ferroan nontronite from the Red Sea geothermal system. *Clays and Clay Minerals*, v. 20, p. 217-223.
- Bischoff, J. L. and Sayles, F. L., 1972, Pore fluid and mineralogical studies of recent marine sediments: Bauer Depression region of East Pacific Rise. *Jour. Sed. Pet.*, v. 42(3), p. 711-724.
- Bonatti, E., Kraemer, T. and Rydell, H., 1972, Classification and genesis of submarine iron-manganese deposits. In D. R. Horn (ed.), *Papers from a conference on ferromanganese deposits on the ocean floor* (unpublished), NSF IDOE.
- Burns, R. G., 1965, Formation of Cobalt (III) in the amorphous  $\text{FeOOH} \cdot n\text{H}_2\text{O}$  phase of manganese nodules. *Nature*, v. 4975, p. 999.
- Burns, R. G. and Brown, B. A., 1972, Nucleation and mineralogical controls on the composition of manganese nodules. In D. R. Horn (ed.), *Papers from a conference on ferromanganese deposits on the ocean floor* (unpublished), NSF IDOE.

- Burns, R. G. and Fuerstenau, D. W., 1966, Electron-probe determinations of inter-element relationships in manganese nodules. *Am. Min.*, v. 51, p. 895-902.
- Chester, R. and Hughes, M. J., 1967, A chemical technique for the separation of ferromanganese minerals, carbonate minerals and adsorbed trace elements from pelagic sediments. *Chem. Geol.*, v. 2, p. 249-262.
- Church, T. M., 1970, Marine barite. Ph.D. dissertation, Scripps Institution of Oceanography, University of California, San Diego.
- Cronan, D. S. and Tooms, J. S., 1969, The geochemistry of manganese nodules and associated pelagic deposits from the Pacific and Indian Oceans. *Deep-Sea Res.*, v. 16, p. 335.
- Dasch, E. J., Dymond, J. R. and Heath, G. R., 1971, Isotopic analysis of metalliferous sediment from the East Pacific Rise. *Earth Planet. Sci. Lett.*, v. 13(1), p. 175-180.
- Drake, M. J. and Weill, D. F., 1972, New rare earth element standards for electron microprobe analysis. *Chem. Geol.*, v. 10, p. 179-181.
- Dymond, J. R., Corliss, J. B., Heath, G. R., Field, C. W., Dasch, E. J. and Veeh, H. H., 1973, Origin of metalliferous sediments from the Pacific Ocean. *Geol. Soc. Am. Bull.*, (in press).
- El Wakeel, S. K. and Riley, J. P., 1961, Chemical and mineralogical studies of fossil red clays from Timor. *Geochim. et Cosmochim. Acta.*, v. 24, p. 260-265.
- Frondel, C., Marvin, U. B. and Ito, J., 1960, New occurrences of todorokite. *Am. Min.*, v. 45, p. 1167-1173.
- Goldberg, E. D., 1954, Marine geochemistry I. Chemical scavengers of the sea. *J. Geol.*, v. 62, p. 249-265.
- Kerr, P. F. et al., 1951, Analytical data on reference clay minerals. In Preliminary Reports, Reference Clay Minerals. American Petroleum Institute.

- Herron, E. H., 1972, Sea-floor spreading and the Cenozoic history of the East-Central Pacific. *Geol. Soc. Am. Bull.*, v. 83, p. 1671-1692.
- Horn, D. R., Horn, B. M. and Delach, M. N., 1972, Ferromanganese deposits of the North Pacific. NSF IDOE Technical Report No. 1, NSF GX-33616.
- MacEwan, D. M. C., 1961, Montmorillonite minerals. In G. Brown (ed.), *The X-ray identification and crystal structures of clay minerals*. Mineral. Soc. London, 1961, p. 156-157.
- Margolis, S. V., 1973, Micro-laminations in marine manganese nodules as revealed by electron microscopy. In Inter-university program of research on ferromanganese deposits of the ocean floor, Phase 1 Report. (unpublished) National Science Foundation, IDOE, p. 77-85.
- Mehra, O. P. and Jackson, M. L., 1958, Iron oxide removal from soil and clays by a dithionite-citrate system buffered with sodium bicarbonate. *Clays and Clay Minerals*, v. 5, p. 317-327.
- Menard, H. W., 1964, *Marine geology of the Pacific*. McGraw-Hill, New York, p. 173.
- Osthaus, B. B., 1954, Chemical determination of tetrahedral ions in nontronite and montmorillonite. In *Clays and Clay Minerals*, Nat. Acad. of Sci.-Nat. Res. Council, Publ. 327, p. 404-417.
- Piper, D. Z., 1972, Rare-earth elements in manganese nodules from the Pacific Ocean. In D. R. Horn (ed.), *Papers from a conference on ferromanganese deposits on the ocean floor*. (unpublished) p. 123-131.
- Revelle, R. R., Bramlette, M., Arrhenius, G. and Goldberg, E. D., 1955, Pelagic sediments of the Pacific. *Geol. Soc. Am. Spec. Paper* 62, p. 221-235.
- Riley, J. P. and Sinhaseni, P., 1958, Chemical composition of three manganese nodules from the Pacific Ocean. *Jour. Mar. Res.*, (Sears Found. Mar. Res.), v. 17, p. 466-482.
- Ross, C. S. and Hendricks, S. B., 1945, Minerals of the montmorillonite group. U. S. G. S. Prof. Paper 205-B.

Rucklidge, J. and Gasparri, E. L., 1968, Geology Dept. Report "EMPADR" University of Toronto, Toronto.

Sorem, R. K., 1960, X-ray diffraction technique for small samples. Am. Min., v. 45.

Sorem, R. K. and Foster, A. R., 1972, Internal structure of manganese nodules and implications in beneficiation. In D. R. Horn (ed.), Papers from a conference on ferromanganese deposits on the ocean floor. (unpublished) NSF IDOE, p. 167-183.

Straczek, J. A., Horem, A., Ross, M. and Warshaw, C. M., 1960, Studies of the manganese oxides. IV. Todorokite. Am. Min., v. 45, p. 1174-1184.

Sweatman, T. R. and Long, J. V. P., 1969, Quantitative electron-probe micro-analysis of rock-forming minerals. Journ. Petrol., v. 10(2), p. 332-379.